Physics and Engineering
of
Sheet Plasma Devices

A dissertation submitted in partial fulfillment
of the requirements for the degree of
Doctor of Engineering

The Graduate School of Science and Engineering
Doshisha University

Arnold Rey B. Gines

Kyoto, Japan
June, 2019

Synopsis

Sheet plasmas have the advantage of producing thin films and functional surfaces by generating localized high-density and temperature gradient regions suitable for specific reactions. A stream of high energy electrons from a plasma cathode efficiently excites and/or ionizes atomic and molecular species which are confined in a linear magnetic field. An electron cyclotron resonance (ECR) sheet plasma device employing a 2.45 GHz microwave source and combination of permanent magnets and field coils was designed and operated. The combined field realized a linear magnetic field that sustained a rectilinear confinement of the plasma.

In Chapter 1, a brief introduction is provided to give a short background on the current theoretical understanding of magnetized sheet plasma devices. Chapter 2 focuses on the device description and initial conditions of the generated plasma. The design of the whole system was explained. In addition, techniques for plasma diagnostics and analysis of the plasma discharge were described.

In Chapter 3, a more detailed description of the plasma discharge was carried out. Using Langmuir probe, the plasma was analysed to understand its behaviour relative to different operating parameters and vacuum conditions. ECR condition was achieved using the combined field from permanent magnets and field coils. The overall performance of the plasma operated at sub-ECR and ECR conditions were compared.

A localized heating was observed under high power operation which limits the device performance. A local gas injection was designed to supply gas directly to the cathode region. In Chapter 4, the device performance with the new gas inlet design was compared with that of the usual gas introduction directly to the main chamber. Particularly observed was the stable and longer operation time in the "local gas injection" mode up to 3 kW microwave power. Plasma parameters were observed in Chapter 5 with consideration of the effect of the magnetic field. The effect of the applied magnetic field to the plasma profile using electron temperature, electron density, plasma potential, floating potential and ion saturation was described in more detail. Images of the plasma was used to support observation made from plasma parameters. Meanwhile, low frequency plasma instabilities were observed at high magnetic flux density and was briefly discussed.

In Chapter 6, observation of high energy electrons in a hot cathode-type sheet plasma was presented. A plasma cathode excited a millimeters thick sheet plasma throughout a 92 cm long chamber in a 270 G linear static magnetic field. Electron energy probability functions measured for Ar plasmas by an electrostatic probe indicated the presence of high energy electrons in the produced plasma. The high energy electron component occupied the substantial part of the electron energy distribution function at lower plasma operating pressure. Electrical bias voltage applied to the electrode terminating the plasma flow determined the plasma space potential.

Table of Contents

List of Figures

Chapter 1

Introduction

1.1 Overview

A weakly ionized plasma opens new ways to synthesize materials and modify surface structures [1]. Sheet plasmas have the advantage of producing thin films and functional surfaces by generating localized high-density and temperature gradient regions suitable for specific reactions. A stream of high energy electrons from a plasma cathode efficiently excites and/or ionizes atomic and molecular species which are confined in a linear magnetic field [2, 3]. The so called Uramoto-type sheet plasma device employs one of the simplest design to realize a sheet-shaped plasma by combining a linear magnetic field produced by electromagnets and a pair of dipole permanent magnets [4]. Because of the performance to create a thin plasma, the configuration was utilized among several research groups [5-7].

Since the original invention by Uramoto, sheet plasma devices have been developed to improve their performance specifically as H^- ion sources. Ando *et al.* attempted to increase high energy electron density in the plasma by employing reflex type cathodes [8], while Tonegawa added a gas supply system to realize a hydrogen flow across the plasma sheet [9]. Noguera and Ramos confirmed the effectiveness of Ar and Mg addition into their sheet plasma for H^- ion extraction [10,11]. Meanwhile, Noguera and Ramos also applied the same sheet plasma device for nitride coating [12]. They utilized efficient production of excited molecules in sheet plasma by high energy electrons to realize better plasma system for materials processing [13]. A major achievement of the process was that it did not require substrate heating to promote TiN coating of stainless steel. Mechanical tools requiring reinforced surface hardness such as drill bits, punchers and taps were surface coated utilizing the sheet plasma device.

The development of coating systems of structure components is vital in addressing structural corrosions accelerated by environmental damages affecting the functionality of the subjected parts. In certain geographical regions where severe environmental conditions may occur, the application of surface coatings technology to certain materials could provide solutions to common wear and tear problems and material degradation of components exposed to environmental conditions such as high humidity, prolonged solar radiation, even ambient chemical reactions and unwanted biological processes. In regions where environmental factors play a huge role in material degradation like, the need for the adaption of surface coating technologies becomes relevant. With the growing number of climate-related concerns in the development of certain technologies, the need to enhance component parts and materials must be an integral part.

This dissertation provides an account of the development and diagnostics of sheet plasma device systems. First, a 2.45 GHz microwave sheet plasma device that features several novel parts was operated and characterized. The system was designed to produce stable sheet-shaped plasma with high density and temperature gradient over a range of plasma input parameters The device design aims to resolve a number of plasma operation limitations encountered in such devices. Second, a duoplasmatron-type source sheet plasma device was operated to observe the emergence of more energetic electrons.

1.2 Objectives and motivations

Sheet plasmas have the advantage of being utilized in a number of surface processing applications due to the plasma discharge’s unique geometric configuration. A stream of dense plasma generated over an area is suitable for a variety of material surface processing and large area process applications. Some of the prospective applications include fabrication of functional thin films, coating protection and circuit board coatings, anti-adherent coatings, superhydrophobic coatings, self-cleaning and antimicrobial surfaces.

Surface coatings and thin film synthesis require precise operation conditions according to specified surface technology applications. Despite existing surface processing technologies, certain limitations to full realization of sheet plasma application must be overcome. Surface structures fabrication and surface technologies require precise methodologies tailored to process specifications.

The development and diagnostics of magnetized plasma devices aim to improve the operation conditions of sheet plasma devices by studying the effect of employing novel device components. The study also aims to understand the plasma condition, such as plasma and operation parameters to determine the sheet plasma dimensions, in the produced sheet plasma for a given operation condition and derive optimization parameters and conditions for future industrial applications. As such, this research attempts to contribute to the development and understanding of sheet plasma devices for surface technology applications.

1.3 Organization

Beginning in Chapter 2, the section introduces some fundamental theory on plasma processes and related sheet plasma design and operation and an introductory theory on thin films and surface coating technology. Initial plasma operation conditions and diagnostic techniques involving Langmuir probe (LP), optical emission spectroscopy (OES) and plasma image analysis are briefly discussed. In Chapter 3, more detailed description of the device and operation parameters for stable plasma discharge are presented. In Chapter 4, the effect of adding a localized gas injection to feed gas in the quartz window region is discussed. Heating up of the cathode region leading to a damaged microwave window and its seals was observed and has been an issue in the initial device design. In this chapter, a modified microwave window design aims to rectify the residual heating as a consequence of high microwave power operation. For Chapter 5, sheet plasma is characterized with respect to the applied magnetic field. Plasma profiles in terms of several plasma parameters are described from varying magnetic. Plasma instabilities observed during operation are briefly presented. In Chapter 6, observation of high energy electrons in a duoplasmatron cathode-type sheet plasma device is present. Investigation of the electron energy probability function reveals population of high energy electrons in the sheet plasma discharge as a result of applying voltage bias to the terminal walls. Finally, a summary of all the findings is presented in Chapter 7 with several recommendations for possible prospective research endeavors related to this study.

References

[1] S. Dou, L. Tao, R. Wang, S.E. Hankari, R. Chen, S. Wang, Advanced Materials, **30**, 1705850 (2018).

[2] M. Wada, S. Takeshima, H. Tsuda, M. Sasao, Rev. Sci. Instrum. **61**, 430 (1990).

[3] Y. Abate, H.J. Ramos, Rev. Sci. Instrum. **71**, 3689 (2000).

[4] J. Uramoto, Shinku (in Japanese), **25**, 719 (1982).

[5] K. Jimbo, M. Iima, Rev. of Sci. Instrum. **66**, 1035 (1995).

[6] K. Nakase, T. Shibata, T. Yasui, H. Tahara, T. Yoshikawa, Thin Solid Films **281-282**, 152-154.

[7] K. Shibata, N. Yugami, Y. Nishida, Review of Scientific Instruments **65**, 2310 (1994).

[8] J. Uramoto: AIP Conference Proceedings, 158, 319 (1987).

[9] A. Ando, T. Kuroda, Y. Oka, O. Kaneko, A. Karita, T. Kawamoto: Rev. Sci. Instrum. **61**, 442 (1990).

[10] A. Tonegawa, K. Kumita, M. Ono, T. Shibuya, K. Kawamura: Jpn. J. Appl. Phys. **45**, 8213 (2006).

[11] V.R. Noguera, H. J. Ramos: IEEE Trans. Plasma Sci. **36**, 1416 (2008).

[12] V.R. Noguera, G.Q. Blantocas, H. J. Ramos: Nucl. Instrum. Methods, B-**266**, 2627 (2008).

[13] V.R. Noguera, H. H. Ramos: Thin Solid Films, **506-507**, 613 (2006).

Chapter 2

Design and Operation of a 2.45 GHz Microwave Sheet Plasma Device

2.1 Introduction

A large number of first generation plasma sources utilize the production mechanism of thermionically excited discharges involving hot cathodes (e. i. filaments) to extract electrons that are then accelerated across an applied potential. Energy transfers from the primary electrons are promoted via a series of inelastic collisions. To limit losses from electrons diffusing on confinement walls and device surfaces, magnetic fields are employed to contain the plasma as well as shape them to any desired profile or configuration. Trapping of the charged particles improves power efficiency by thermalizing the hot primary electrons with the colder secondary electrons by ionization.

One of the aims of magnetized plasma devices is to produce high electron density to around 10^{18} m^{-3} while minimizing the effects of any localized heating observed at high input powers over a period of stable operation. The high density region realizes rapid sputtering of target materials utilized for deposition of the sputtered material to form functional surface or film. While material coating and surface technology are poised towards large area production scales to minimize costs and optimize processes, maintaining high purity and uniformity of the output remains a vital requirement. Thus, sheet plasmas for industrial applications must be developed with consideration of specific process requirements.

Previous studies on sheet plasma devices involve employment of various plasma sources including DC discharges, radio frequency and microwave sources. In DC sources, the ease with which plasma is generated depends on the plasma extraction mechanism. Commonly, a major issue with plasma processing devices includes the observation of unwanted impurities from chamber parts such as cathode filament that are made of metals like tungsten. In addition, the lifetime of physical parts inside the process chamber requires that the inside be maintained to the same configuration over all processes. As filaments burn out at long operation, the need to replace these parts are an additional consideration when designing plasma sources.

In microwave plasma, ionization arises from the electrons' response to time-varying electric field. When a sufficient number of electrons are accelerated, discharge can be sustained. The application of microwave plasma for treatment of surfaces and bulk materials proves to be more effective than DC and RF plasmas due to production of more dense active plasma species [1]. In microwave discharges, electron temperature and number density are higher because of power coupling through radiation bypassing sheath losses[2]. Furthermore, plasma operation over a wider range of gas pressure is possible, which when combined with greater electron temperature provides the ability to produce higher fraction of ionization and dissociation [3].

This chapter presents the full device set-up of a 2.45 GHz microwave sheet-shaped plasma system. A basic plasma theory is given at first. System components are presented briefly after this section with a discussion of the magnetic field configuration. Experimental tools used to diagnose the system are also briefly mentioned.

2.2 Sheet plasma system

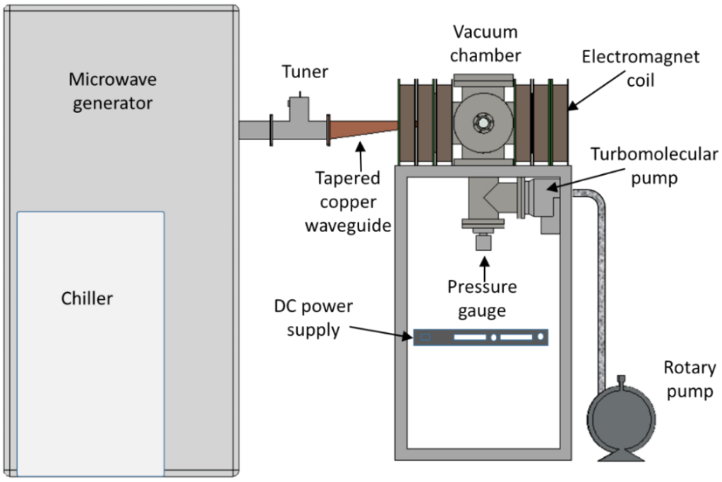

Figure 2.1: Schematic diagram of the sheet plasma device system.

Figure 2.2: Photo of the actual sheet plasma set up.

The general schematic of the microwave sheet plasma system is illustrated in Figure 2.1 while a photo of the actual device is shown in Figure 2.2. The system at the time of this report is housed in the Global Resource Management common room in Hochikan building at Doshisha University, Kyotanabe Campus. The device is composed of the following main part: stainless steel vacuum chamber, 2.45 GHz microwave source coupled to an EH tuner, copper waveguide, pancake coils coupled to a DC source, permanent magnets (not visible), vacuum pumps composed of a turbomolecular pump and dry scroll pump, full range pressure gauge and a water-cooled chiller.

2.2.1 Vacuum chamber

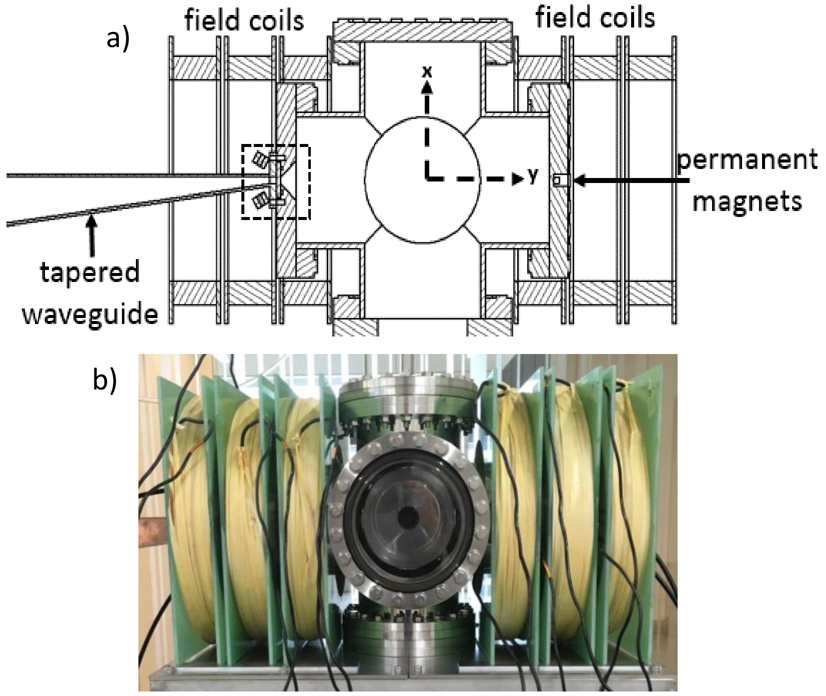

Figure 2.3: a) Schematic of the chamber region with a reference coordinate axis with origin at the center the chamber, and b) the actual vacuum chamber with a large viewport.

The main vacuum chamber is made of a standard stainless steel six-way crosses flange as shown in Figure 2.3. For clarity, a Cartesian coordinate is set at the center of the vacuum chamber as illustrated in Figure 2.3a). The tubular body has length of around 30 cm and inner diameter of 14.7 cm. Each face fits a standard CF 203 stainless steel flange. The vacuum system is appended at the bottom flange. Another face is fitted with a full viewport, as seen in Figure 2.3b) to provide a lateral profile view of the plasma. An aluminum mesh is fitted to the viewport to shield the region from possible microwave leakage.

2.2.2 Power supplies

A 2.45 GHz (TE-MG3000) microwave power source from *Tamaoki Electronics Co., Ltd.*, supplies the required electromagnetic radiation. It has a maximum power output of 3 kW and is delivered to the chamber through a tapered copper waveguide and a 110 mm by 7 mm quartz glass window. It comes with an EH tuner which can be manipulated to minimize power reflection. For the electromagnetic coils, a *Kikusui* regulated DC power supply feeds the current of up to 15 A at 100 V maximum.

2.2.3 Magnetic field sources

The fundamental force of magnetism plays huge role in the overall behavior of ionized matter such as plasma. The control of shape and configuration of high-density plasmas are important in industries utilizing plasma technologies for materials fabrication and development of functional surfaces. The rectangular shape of sheet plasmas are produced by magnetic fields from current-carrying coils or permanent magnets strategically placed around the plasma-containing vacuum chambers.

2.2.3.1 Magnetic coils

Six magnetic coils, as shown in Figure 2.4, are employed for the magnetic confinement of the generated plasma forming into a sheet configuration. The coils consist of 3 mm diameter enamel-coated copper wires wound, to initially unknown number of turns, on a PVC frame and are electrically connected in series fed by a variable output power supply. In this study, the coil current is limited to 15 A to limit the heating up of the metal wires. A cooling fan is used to cool the coils at high coil current over long operation. In Figure 2.5, given an applied coil current, *I* (flow of current shown in red arrow), the field induced in the chamber is graphically represented by the black lines with arrows moving across and within the loops of coils. The linear magnetic field through the loops is responsible for the rectangular shape of the plasma discharge. Here, the magnetic field is described in terms of the magnetic flux density, B and is calculated and compared with the measurements. A Hall probe coupled to a *Lakeshore Model 460* 3-channel gauss meter measures the field along the y-axis.

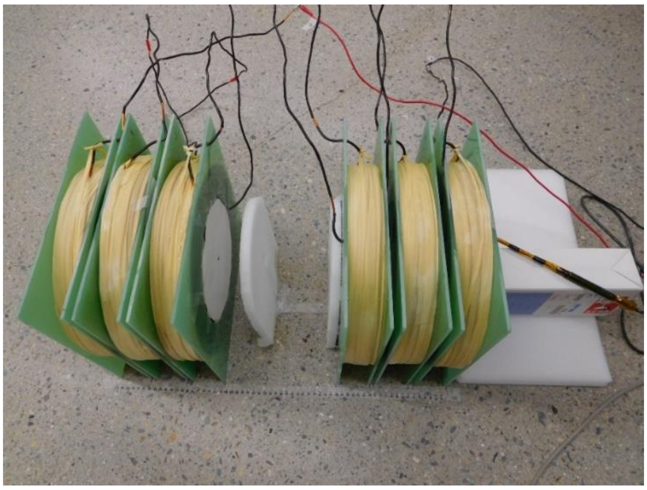

Figure 2.4: Six pancake coils employed in the sheet plasma device.

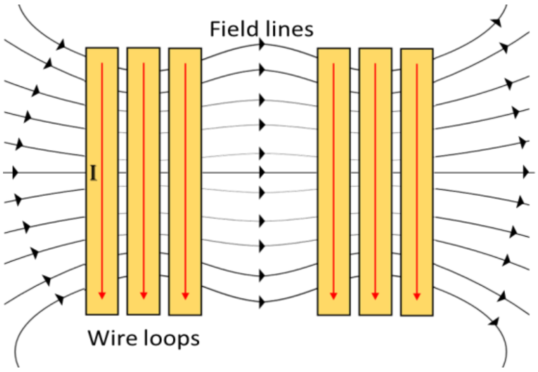

Figure 2.5 : Graphic illustration of magnetic field lines due to the six pancake coils.

Consider a current-containing circular loop with radius, R, similar to a single loop in the field coils in Figure 2.6. An axis is defined in the space containing the field coils for clarity. From Biot-Savart law, the strength of the field $\vec{B}$ of a wire coil at any point along the y axis is given by the equation,

$$dB_y = \frac{\mu_o I dL}{4\pi}\frac{R}{(y^2+R^2)^{3/2}} \tag{2.1}$$

Integrating over the entire coil gives the total flux density from the coil at a given point,

$$B_y = \frac{\mu_o I}{4\pi}\frac{2\pi R^2}{(y^2+R^2)^{3/2}} \tag{2.2}$$

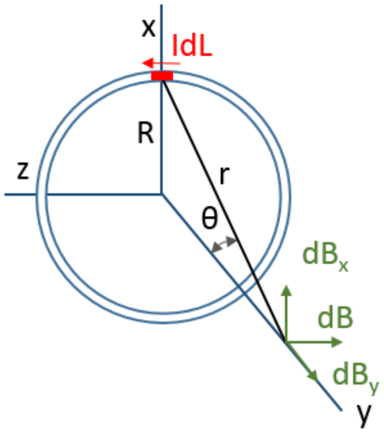

Figure 2.6: Magnetic flux density from a current carrying wire.

The derived equation in (2.2) can be used to calculate B at any point on the y-axis, which is set to be the central horizontal axis in the vacuum chamber, to derive the total

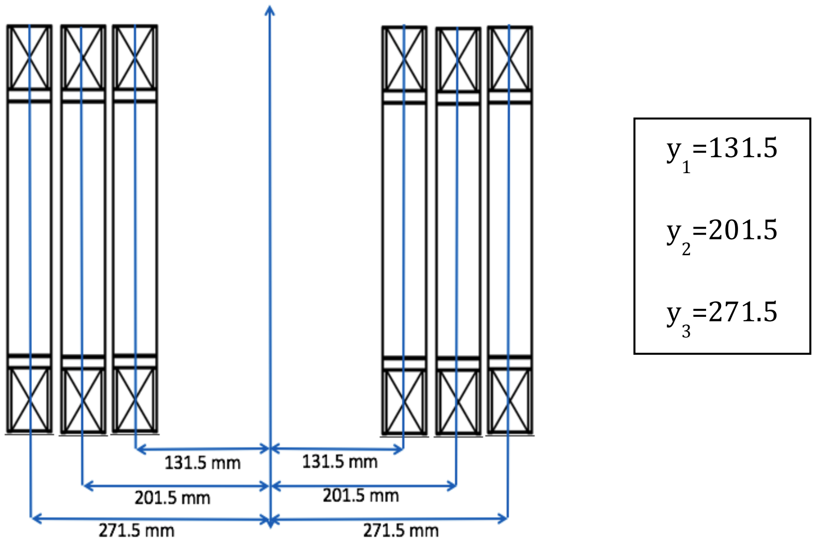

Figure 2.7: Schematic diagram of the magnetic coils' relative position.

contribution of all the field coils. The estimation is done by considering the coil as a thin wire where all of the windings are concentrated in the center of the coils for simplicity.

Before calculating B along the y-axis, first, the positions of the six coils are defined with respect to the center of each pair of coils as shown in the Figure 2.7. Using these positions and equation (2.2), the total field at any point z along the y-axis is given by (2.3). The total current, I, is equivalent to Ni where N is the total number of turns of each coil and i is the applied current in the coils. Using the "thin wire approximation", the coil radius is set at 0.135 m. For this study, the actual total number of turns for each coil is unknown. As such, all the coils are assumed to have the same number of wire turns, N.

$$B_y = \frac{\mu_o I}{2}\left\{\begin{array}{c} \frac{r^2}{[[r^2+(y+y_1)^2]]^{\frac{3}{2}}} + \frac{r^2}{[r^2+(y+y_2)^2]^{\frac{3}{2}}} + \frac{r^2}{[r^2+(y+y_3)^2]^{\frac{3}{2}}} + \\ \frac{r^2}{[r^2+(y-y)^2]^{\frac{3}{2}}} + \frac{r^2}{[r^2+(y-y_2)^2]^{\frac{3}{2}}} + \frac{r^2}{[r^2+(y-y_3)^2]^{\frac{3}{2}}} \end{array}\right\} \qquad (2.3)$$

The above expression is used to approximate the magnetic flux density along the y-axis. Considering an input current of 6 A, the calculated field are plotted in Figure 2.8 along with the actual measurements. The induced field is symmetric with respect to the horizontal axis. B_y is maximum along the center coil of each set of three implying stronger magnetic field at this region. For the calculated B_y, the number of turns of each coil was initially set at 200 based from the approximation gathered from the coils' geometry. However, the calculated and observed field differ by around 20 G. This suggests higher total number of turns for each coil.

The determination of the estimated total number of turns in a coil can be done by employing chi-squared (χ^2) test. It is used to determine the minimum difference between the expected values and the observed values. By taking the chi-squared values of each point on the calculated and actual measurement and plotting their values for different number of turns, the number of turns that achieves the minimum value of chi-squared can be determined, from Figure 2.9, that when N=246, χ^2 is minimized. This value can be used to estimate the magnetic flux density along the y-axis. The accuracy of N can be confirmed by considering a different coil configuration and comparing the calculated and measured values of B_y.

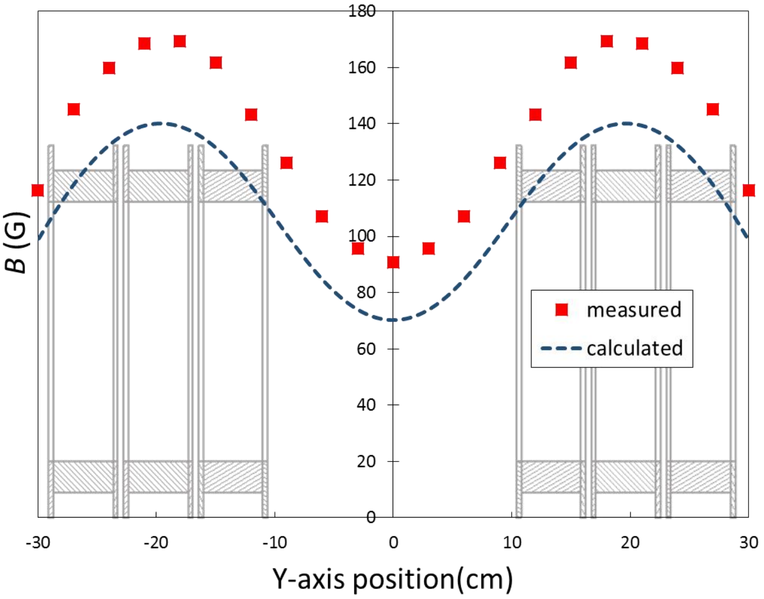

Figure 2.8: At 6 A coil current, comparison between the calculated and measured total magnetic flux density along the center horizontal axis of the magnetic field coils when the number of coil turns is set at N=200.

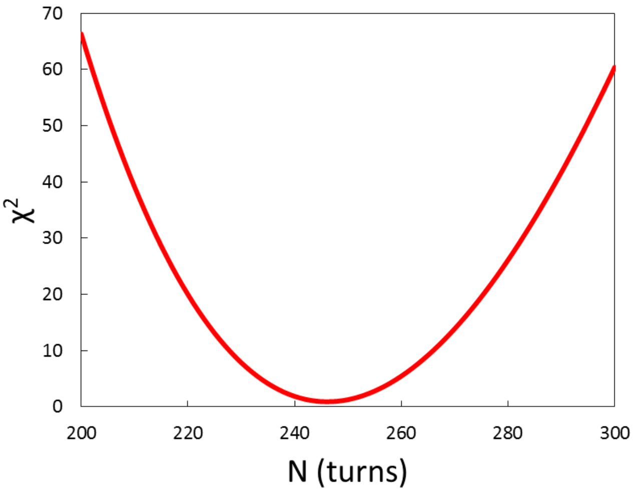

Figure 2.9: χ^2 versus number of turns, N.

To confirm this approximation, the magnetic coils were moved farther apart as illustrated in Figure 2.10. From the original set-up, the two coils closest to the center were maintained to the same position while the other two pairs were moved farther away from the vertical center. Using this coil configuration, the calculated and the measured field using the approximated number of turns of each coil were compared. The plot in Figure 2.10 of the calculated and the measured B confirms that the estimation of the number of turns arrives at a fairly close approximation. Thus, this confirms that the number of wire turns is about 246.

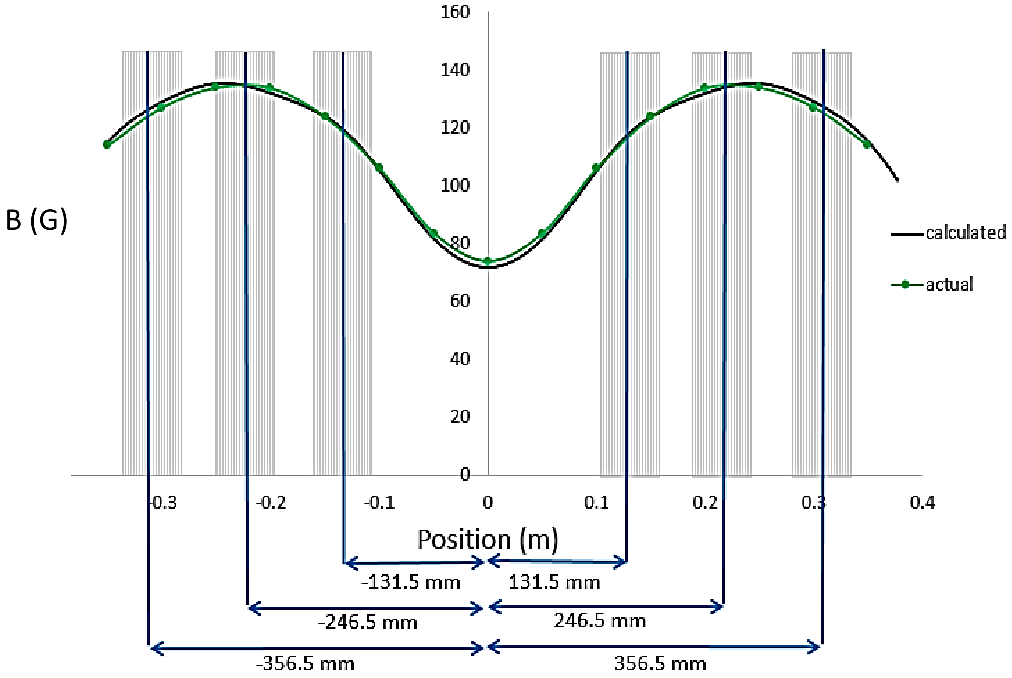

Figure 2.10: Magnetic flux density comparison of the calculated and measured values at 6 A coil current when the coils are oriented accordingly.

Figure 2.11 shows plot of calculation of B for varying coil currents. The plot shows a general increase in flux density as the current is increased. Within the area of interest in the vacuum chamber, as shown in the graph's background, the field is minimum at the center, y=0. Note that the profile agrees with the graphical illustration of the field in Figure 2.5.

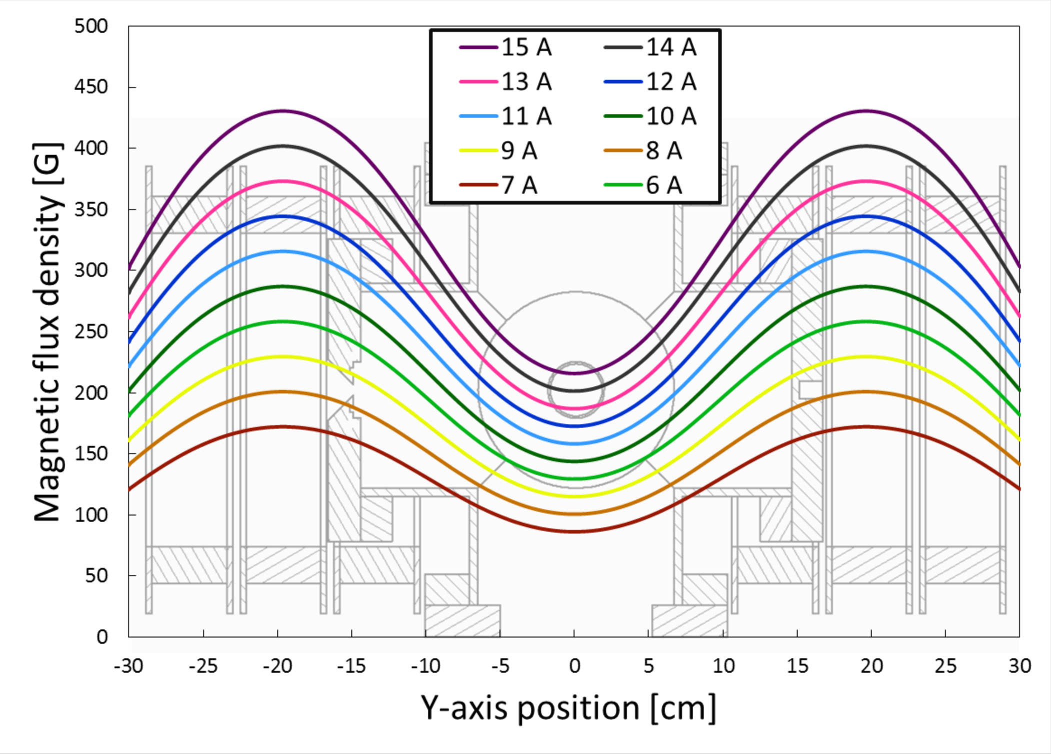

Figure 2.11: Magnetic flux density calculation at varying coil current.

2.2.3.2 Permanent magnets

Figure 2.12 shows the actual permanent magnets installed on the copper waveguide in the cathode region. The addition of the permanent magnets, together with the field coils, are intended to generate a localized electron cyclotron resonance (ECR) condition inside the vacuum chamber near the quartz window. Each neodymium permanent magnets has dimensions 12 cm by 1.2 cm by 0.5 cm. Based on manufacturer's specification, each magnet has surface magnetic flux density of 2530 G. Due to the high intrinsic strength of the magnets, a frame made of aluminum encases the permanent magnets to the configuration shown in Figure 2.12. The sets of permanent magnets are installed and tilted at 45 degree angle towards the central vertical axis of the chamber as illustrated in Figure 2.13. A stopper on top of the waveguide compensates for the asymmetrical shape of the medial cross-section of the copper waveguide and positions the magnets symmetrically with respect to the horizontal center of the chamber.

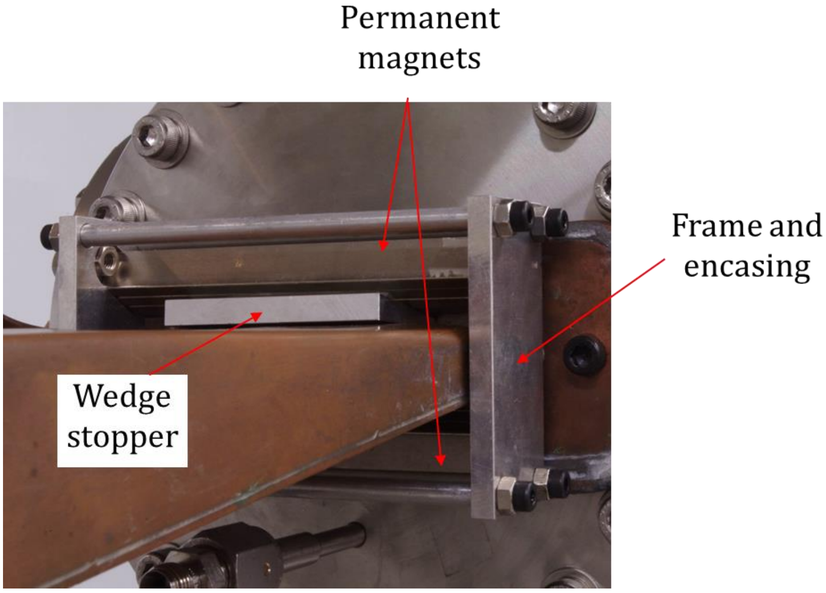

Figure 2.12: Details of the permanent magnets installed on the copper waveguide.

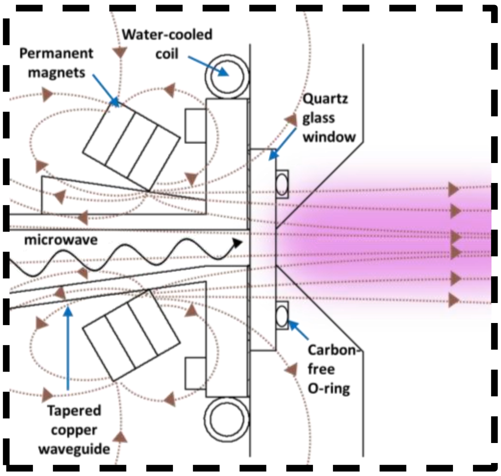

Figure 2.13: Details of the tapered copper waveguide with the installed magnets.

In Figure 2.14, the measured magnetic flux density emanating from the permanent magnets, depicted in Figure 2.13, along the central horizontal axis inside the chamber is shown. The plot of *B* shows strong field when approaching the quartz glass window surface and decays rapidly towards the center of the chamber where it is almost zero. The combination of the permanent magnets and the field coils generate field across the chamber where the maximum *B* is always observed in the vacuum-face of the quartz glass window. The generation of a local electron cyclotron resonance (ECR) region is achieved a few mm from the quartz window.

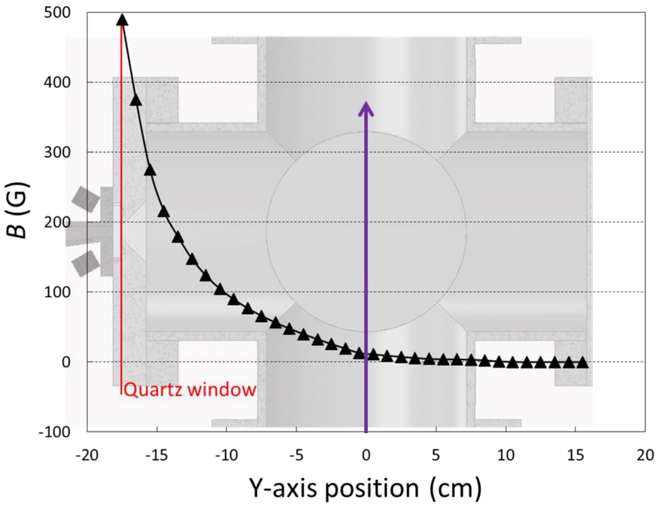

Figure 2.14: Measured magnetic flux density along the central horizontal axis of the chamber from the permanent magnets.

Another set of weaker permanent magnets is installed in the terminal wall, opposite flange to the microwave window, to enhance the expansion of the sheet plasma across the entire drift axis. However, in this report, the effect of such feature to the behavior of the plasma has not been investigated.

2.2.4 Cut-off frequency

The wave propagation in a magnetized plasma is governed by the following three Maxwell's equations:

$$\mathbf{\nabla} \times \mathbf{E} = -\frac{\partial \mathbf{B}}{\partial \mathrm{t}} \tag{2.4}$$

$$\mathbf{\nabla} \cdot \mathbf{E} = \frac{\rho}{\epsilon_{\mathrm{o}}} \tag{2.5}$$

$$\mathbf{\nabla} \times \mathbf{H} = \mathbf{j} + \epsilon_{\mathrm{o}} \frac{\partial \mathbf{E}}{\partial \mathrm{t}} \tag{2.6}$$

From (2.4),

$$\mathbf{\nabla} \times (\mathbf{\nabla} \times \mathbf{E}) = -\frac{\partial}{\partial \mathrm{t}} \mathbf{\nabla} \times \mathbf{B} \tag{2.7}$$

In vacuum, $\mathrm{j} = 0$ and given that $\mathbf{B} = \mu_{\mathrm{o}} \mathbf{H}$,

$$\mathbf{\nabla}(\mathbf{\nabla} \cdot \mathbf{E}) - \mathbf{\nabla}^2 \mathbf{E} = -\mu_{\mathrm{o}} \epsilon_{\mathrm{o}} \frac{\partial^2 \mathbf{E}}{\partial \mathrm{t}^2} \tag{2.8}$$

Since $\mathbf{\nabla}(\mathbf{\nabla} \cdot \mathbf{E}) = 0$

$$\frac{\partial^2 \mathbf{E}}{\partial \mathrm{t}^2} = -\frac{1}{\mu_{\mathrm{o}} \epsilon_{\mathrm{o}}} \nabla^2 \mathbf{E} = \mathbf{c}^2 \nabla^2 \mathbf{E} \tag{2.9}$$

where $\mathrm{c} = \frac{1}{\sqrt{\mu_{\mathrm{o}} \epsilon_{\mathrm{o}}}}$, corresponding to the light speed.

In plasma, $\mathrm{j} = -e n_e v_e$, again, from (2.4)

$$\mathbf{\nabla} \times (\mathbf{\nabla} \times \mathbf{E}) = -\frac{\partial}{\partial \mathrm{t}} \mathbf{\nabla} \times \mathbf{B} \tag{2.10}$$

$$\mathbf{\nabla} \times (\mathbf{\nabla} \times \mathbf{E}) = -\mu_{\mathrm{o}} \frac{\partial}{\partial \mathrm{t}} (\mathbf{j} + \epsilon_{\mathrm{o}} \frac{\partial \mathbf{E}}{\partial \mathrm{t}}) \tag{2.11}$$

$$\mathbf{\nabla} \times (\mathbf{\nabla} \times \mathbf{E}) = -\mu_o e n_e \frac{\partial v_e}{\partial \mathrm{t}} - \mu_o \epsilon_o \frac{\partial^2 \mathbf{E}}{\partial \mathrm{t}^2} \tag{2.12}$$

From the equation of motion,

$$m_e \frac{\partial v_e}{\partial \mathrm{t}} = -e\mathbf{E} \tag{2.13}$$

$$-\mathbf{\nabla}^2 \mathbf{E} = -\frac{e^2 n_e}{m_e} \mu_o \mathbf{E} - \mu_o \epsilon_o \frac{\partial^2 \mathbf{E}}{\partial \mathrm{t}^2} \tag{2.14}$$

The solution must be in the form,

$$\mathbf{E} = \mathbf{E}_{\boldsymbol{o}} \mathrm{e}^{i(\boldsymbol{k}\cdot\boldsymbol{r} - \omega t)} \tag{2.15}$$

where $\boldsymbol{k}$ represents the wave number vector.

$$-\mathbf{\nabla}^2 \mathbf{E} = \boldsymbol{k}^2 \mathbf{E} \tag{2.16}$$

$$\frac{\partial^2 \mathbf{E}}{\partial \mathrm{t}^2} = -\omega^2 \mathbf{E} \tag{2.17}$$

Returning from (2.9), it simplifies to,

$$\frac{\partial^2 \mathbf{E}}{\partial \mathrm{t}^2} = c^2 \mathbf{\nabla}^2 \mathbf{E} \tag{2.18}$$

Using (2.16) and (2.17), (2.18) transforms to

$$-\omega^2 \boldsymbol{E} = c^2(-k^2)\boldsymbol{E} \tag{2.19}$$

which then reduces to,

$$c = \frac{\omega}{k} \tag{2.20}$$

$$-\boldsymbol{\nabla}^2 \boldsymbol{E} = -\frac{e^2 n_e}{m_e} \mu_o \boldsymbol{E} - \mu_o \epsilon_o \frac{\partial^2 \boldsymbol{E}}{\partial t^2} \tag{2.21}$$

From (2.16)

$$-k^2 \boldsymbol{E} = -\mu_o \epsilon_o \left(\frac{e^2 n_e}{\epsilon_o m_e} \boldsymbol{E} - \omega^2 \right) \boldsymbol{E} \tag{2.22}$$

$$k^2 = -\frac{1}{c^2} \cdot \omega^2 \left(1 - \frac{e^2 n_e}{\epsilon_o m_e \omega^2}\right) \tag{2.23}$$

Assigning the parameter the character ω_{pe}, corresponding to the plasma frequency

$$\omega_{pe} = \frac{e^2 n_e}{\epsilon_o m_e} \tag{2.24}$$

$$k^2 = -\frac{1}{c^2} \cdot \omega^2 \left(1 - \frac{\omega_{pe}{}^2}{\omega^2}\right) \tag{2.25}$$

Rearranging (2.25) yields

$$\frac{\omega^2}{k^2} = -\frac{c^2}{\left(1 - \frac{\omega_{pe}}{\omega^2}\right)} \tag{2.26}$$

Setting the photon velocity, v_{photon},

$$v_{photon} = \frac{\omega}{k} = -\frac{c}{\sqrt{1 - \frac{\omega_{pe}{}^2}{\omega^2}}} \tag{2.27}$$

This implies that the cut-off frequency is at $\omega = \omega_{pe}$. In magnetized plasma, waves with $\omega > \omega_{pe}$ could not propagate across the plasma and are reflected by the medium.

2.2.5 Tapered copper waveguide

A copper waveguide was designed to fit, on one side, a standard rectangular waveguide from the microwave source and a 110 mm by 7 mm microwave window. The waveguide has straight vertical walls with 109 mm width while the bottom wall tapers towards the smaller microwave inlet. The opening on the microwave side has rectangular dimension of 54.6 mm (width) 7 mm (height). The vacuum side is fitted with a water-cooled copper coil to lower the temperature in this region. However, effective cooling is largely limited on the waveguide material due to inadequate conduction with the microwave inlet flange body.

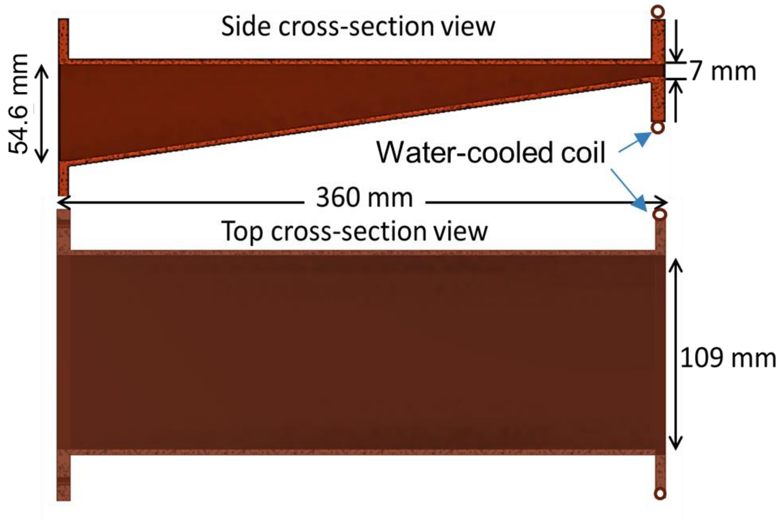

Figure 2.15: Details of the tapered copper waveguide.

2.2.6 Vacuum system

The plasma chamber is evacuated down to below 5×10^{-5} Pa pressure by a 260 *l/s* turbomolecular pump (TMP) that is coupled to an oil-free scroll vacuum pump. A compact FullRange™ gauge measures the chamber pressure positioned underneath the main chamber near the vacuum pump outlet.

During evacuation, the TMP is maintained at 60,000 revolutions per minute (rpm). A typical evacuation time is around 90 minutes for pre-evacuated system while longer evacuation times are necessary when the chamber was exposed to the atmospheric environment before operation. During plasma production, the rotation speed of the TMP is reduced to 23,000 rpm to lower the rate of gas evacuation during plasma operation. Gas is initially introduced though one of the perpendicular faces of the six-way cross chamber (opposite the view port), perpendicular to the direction of the microwave inlet flange.

2.3 Cooling system

A *MTC-1500 Thermo Cool* chiller water-cools the microwave source and the copper waveguide face confronting the cathode region as well as the opposite terminal wall containing the permanent magnets via a leak-free water line. The chiller is kept running during plasma operation and is maintained at 13 ^{o}C. In addition, a cooling fan air-cools the magnetic coils and its surroundings during high current applications on the field coils.

2.4 Electrostatic probe

The ease of application and the wealth of information that can be known on the plasma condition makes Langmuir probe diagnostics a very popular tool for plasma characterization. However, as a physical probe is immersed in the plasma, careful design consideration must be given to limit the amount of interaction of the probe tip's surface with the surrounding plasma.

Typically, a protrusion of wire of known material and dimension immersed in plasma collects information in the form of a current-voltage trace. In this study, a source measure unit was utilized to supply the potential bias on the probe as well as records the measured current. After each voltage sweep, an *I-V* characteristics is generated and stored in a portable drive to be migrated to a personal computer for subsequent analysis and interpretation.

2.4.1 Langmuir probe theory

In plasma, the immersion of a probe creates a phenomenon on its surface wherein an electron or ion rich layer, called "sheath", is formed. As such, quasineutrality (n_e=n_i)

does not hold in the plasma-surface boundary while the relatively high concentration of negative or positive charge can induce high electric fields in the region of the probe, to eventually repel (or attract) charged species resulting in erroneous data.

2.4.2 Langmuir probe design

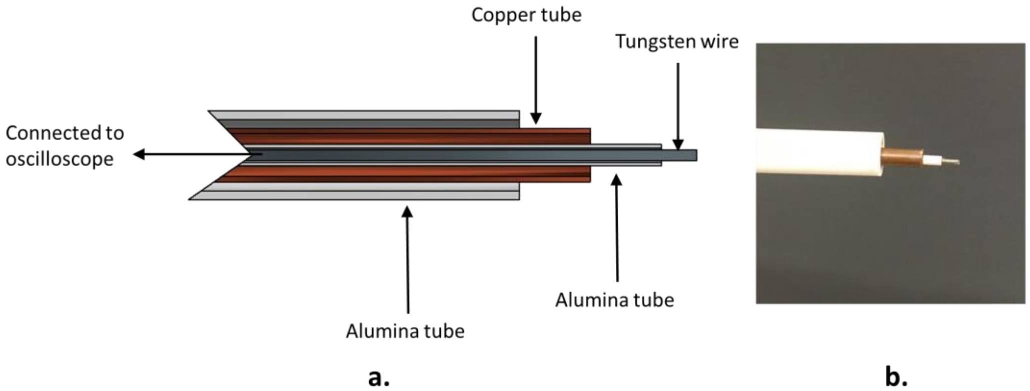

Figure 2.16: a. Schematic diagram of the Langmuir probe cross-section and b. actual image of the single probe.

The cylindrical probe for this study consists of a 0.6 mm diameter tungsten wire enveloped in an alumina tube that leaves a 2 mm exposed end tip of the wire. A grounded copper tube electrostatically shields the probe signal line from ambient noise. A larger alumina tube shields the copper tube and its contents from plasma irradiation and the probe signal noise from electromagnetic irradiation in the chamber. A BNC connector links the probe to a *Yokogawa model GS610* source measure unit which provides the necessary voltage sweep and digitally records the *I-V* curve.

2.4.3 I-V characteristics

In the Langmuir probe analysis, it is assumed that (i) the probe dimension is large enough when compared with the Debye length, (ii) ions in the plasma emanate from great distance with negligible energy and (iii) the probe dimension is small enough relative to the collision mean free path of the plasma

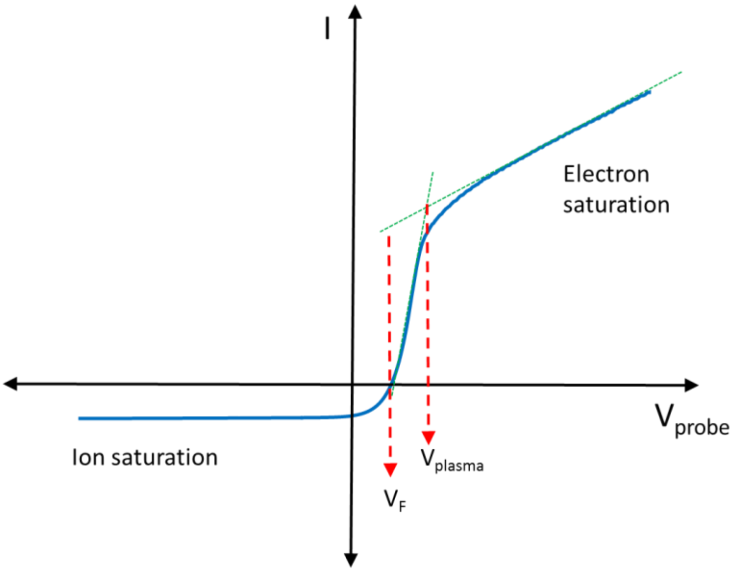

Figure 2.17: a. A sample *I-V* trace measured by a Langmuir probe.

A typical current-voltage characteristics is shown in Figure 2.17. The curve may be divided into three regions according to the probe bias from left to right. From left, as the applied potential (V_{probe}) is increased, the probe attracts positive plasma species and repels electrons. This creates a positive sheath around the probe until it reaches an equilibrium. The left most part of the curve is termed ion saturation where the collected current is called the ion saturation current (I_{sati})and is achieved only when the applied voltage is negative enough to incur a saturated level. As the bias moves towards the less negative region, the ion current decreases until no current is measured. The probe bias corresponding to zero current is called the floating potential (V_F). When V_{probe} is at the $V_{plasma,}$ there is no plasma sheath and the surface of the probe collects the incident ions and electrons. V_{plasma} is generally positive because electrons tend to escape towards the chamber walls faster than ions, which leaves the plasma with a net positive space charge. The electron temperature T_e is taken from the slope of a linear fit from the transition region between V_F and V_{plasma}.

From T_e and I_{sati}, electron density, n_e, can be derived. Moreover, by plotting another linear fit from the $V_{probe}>V_{plasma}$ region, the value of V_{plasma} is determined.

2.5 Optical emission spectroscopy

Optical emission spectroscopy (OES) is a vital tool in plasma diagnostics as it enables the determination of plasma composition as well as the plasmas electrical properties like electron density and its energy distribution function. From plasma collisions, particles are excited to higher energy state and then relaxes to a lower state. During this relaxation, the photons of light is emitted which can be collected and analyzed. The amount of energy encrypted in these photon emission is equal to the difference in energy states of the jump from higher state to lower state. The plasma composition can be described by the relation:

$$\lambda = \frac{hc}{E_p - E_k} \tag{2.28}$$

where h is the Planck's constant, c is the speed of light and E_p and E_k are the higher and lower energy states, respectively. Since the energy transition is characteristic of particle species, plasma composition can be determined from this.

An *Ocean Optics 2000+* optical emission spectrometer coupled to an optical fiber was used to observe the emission spectra from the plasma in the visible light range from 300 nm to 950 nm. It has a spectral resolution of 0.38 nm. The device is connected to a personal computer to display and record the actual emission spectra.

Optical lenses were also used to converge the plasma in cases where very small and specific areas of the plasma needs to be observed. In addition, a variable neutral density filter was used in cases where saturation in the intensity emission plots were observed.

2.6 Plasma observation through a view port

Depending on which region of the plasma discharge is observed, a viewport is installed to a face of the main chamber to capture images and spectra of the plasma. During plasma production, an *RF Explorer Handheld Spectrum Analyzer* detects any microwave leaks from the viewports. No significant amount of frequency from the microwave was detected where the frequency detected goes beyond the threshold value for safe operation.

References

[1] S. Kakizaka, T. Sakamoto, H. Matsura, H. Akatsuka, J. Adv. Oxid. Technol. **10**, 2, 253-259 (2007).

[2] M. Moisan, et al., J. Vac. Sci. Technol. B Microelectron. Nanometer Struct. Process Meas. Phenom. **9**, 1, 8-25 (1991).

[3] I.N. Toumanov, Plasma and High Frequency Processes for Obtaining and Processing Materials in the Nuclear Fuel Cycle. Nova Publishers: New York, USA, 64 (2003).

Chapter 3

Discharge Optimization in an ECR Sheet-Shaped Plasma

In this study, electron cyclotron resonance (ECR) condition is realized by employing a combination of permanent magnets and field coils. The combined fields produce a linear magnetic field that sustained a rectilinear confinement of the plasma. The ECR condition effectively lowered the plasma ignition power to below 500 W and minimum plasma sustaining power, the lowest power that can produce a stable plasma before it extinguishes, to 94 W. The condition also extends the low power ignition to lower gas pressures. At low ignition power, plasma density is greatest along the 0.7-0.3 Pa pressure range. Stable plasma operation at input microwave power of up to 3 kW was achieved without overheating in the quartz window region with the aid of a gas feed mechanism on the quartz window.

3.1 Introduction

To realize a sheet-shaped plasma profile, a linear magnetic field is arranged such that electrons produced in the ionizing region are guided along the field line of force. Among different modes of excitation, microwave-based electron cyclotron resonance

(ECR) enables excitation at lower gas pressure and lower input power while also eliminating high temperature cathodes that introduce impurities into the plasma, thereby, providing greater degrees of freedom on plasma processing parameters. Several techniques may be applied to produce the desired field. Yoshida and Kajinishi [1] employed two coils fed by current of up to 210 A to produce a field equivalent to 1300 G along the discharge chamber and injected a 2.45 GHz microwave power through a quartz glass window. Large current to maintain the magnetic field produce considerable heat which is not ideal for long operations. Morishita *et al.* [2] employed a set of permanent magnets to produce cusp field near the cathode. While a uniform sheet plasma of 20 cm drift length is produced, the fix flux density due to the permanent magnets limits the resulting field profile. Noguera and Ramos [3], and Ramos, *et al*. [4] employed a sheet plasma device with the magnetic field structure similar to the original Uramoto-type sheet to form TiN films for hard coatings applications. Impurity emissions from the plasma cathode often restrict usage of this type of device for any plasma process that forbids introduction of trace impurities.

In this chapter, we investigate the production of sheet-shaped plasma sustained in a moderate intensity magnetic field using a 2.45 GHz microwave source. A localized ECR condition is realized through combining the linear magnetic field produced by a set of coils and a pair of permanent magnets. The discharge conditions satisfying ECR and that with the field intensity for sub-ECR conditions are reported.

3.2 Device set-up

Figure 3.1 illustrates the device set-up with the defined coordinates. Three sets of identical pan-cake coils that are electrically connected in series produce a linear magnetic

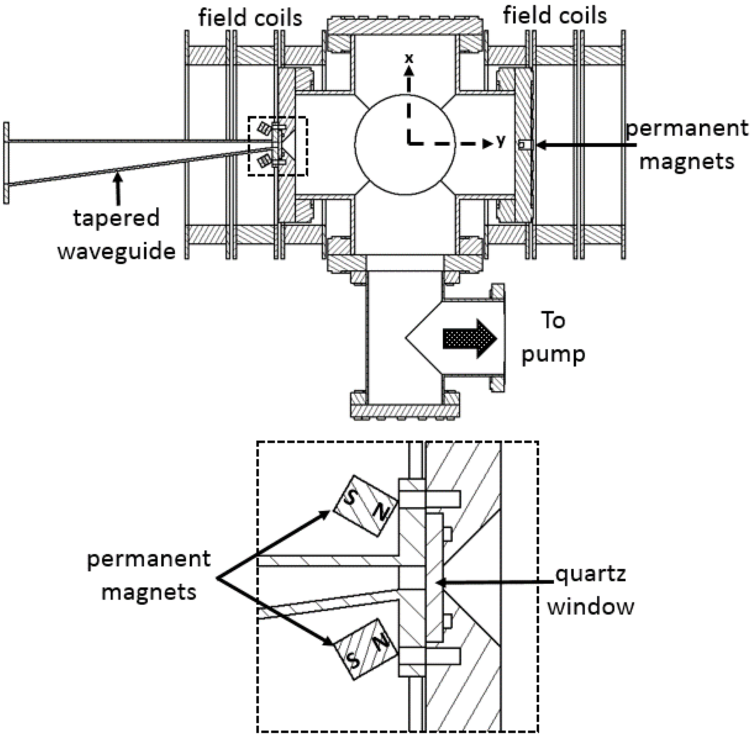

Figure 3.1: Cross-section of the sheet plasma device using permanent magnets and field coils to produce a line cusp field. The inset shows details of the quartz

field with weak magnetic mirrors inside the vacuum chamber. The field strength produced by the coils can be adjusted by controlling the current applied on the coils from a DC source that can provide up to 15 A current. Higher current output was not used to limit the heat produced by the coils over longer period(>1 hour). Figure 3.2 shows the measured field contribution of the coils along the *y*-axis inside the chamber starting from the plasma-facing side of the quartz glass. At 15 A, the field is maximum (430 G) at the quarts window. To realize resonance condition satisfying ECR at B = 875 G, the field is enhanced by the Nd-Fe magnets in the region around the quartz microwave window. These permanent magnets generate cusp field along the y-axis with a maximum flux density of 480 G at the quartz window. When combined with the field coils (at 15 A), the total field generates the intensity corresponding to an ECR region just several millimeters from the quartz window along the axis of the linear magnetic field. The magnetic flux density profiles of the total field from the permanent magnets and the field coils along the chamber axis is also shown in Figure 3.2.

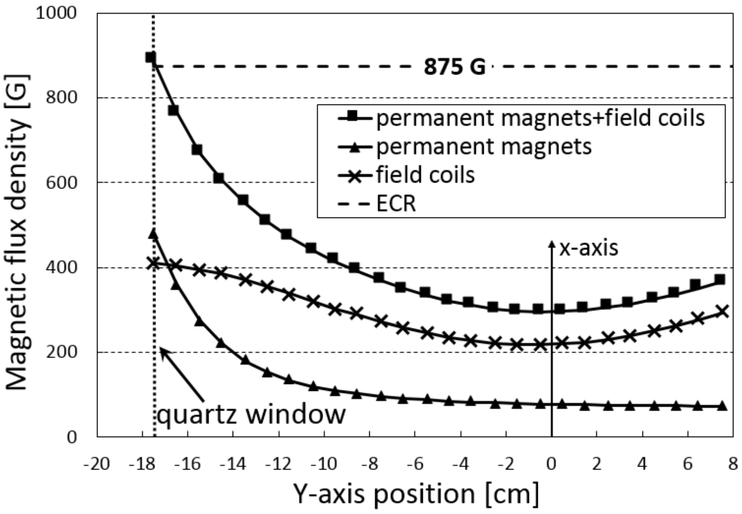

Figure 3.2: Magnetic flux density profile along the downstream central axis inside the chamber. The coil current is 15 A.

Figure 3.3 a) shows the initial microwave inlet flange design. During plasma generation, localized heating was observed in the quartz glass region despite fitting a water-cooling system on the outer face of the flange. A substantial heating was observed at non-ECR conditions. When the microwave power exceeds 1.5 kW, the microwave inlet region considerably heated up to eventually burn the high temperature O-ring seal and damaged the quartz glass. To resolve this overheating problem, a gas inlet feature is incorporated into the flange design as shown as shown in Figure 3.3 b). The gas inlet structure supplies neutral gas in the vicinity of quartz window surface to enhance recombination to aid in cooling down the temperature and density of the local plasma in touch with the window surface realizing the condition similar to a gas divertor [5]. This configuration can sustain plasma excited with up to 3 kW microwave power without damaging the seals and the quartz window for several minutes. The cooling mechanism enables full range of possible microwave power available during this investigation.

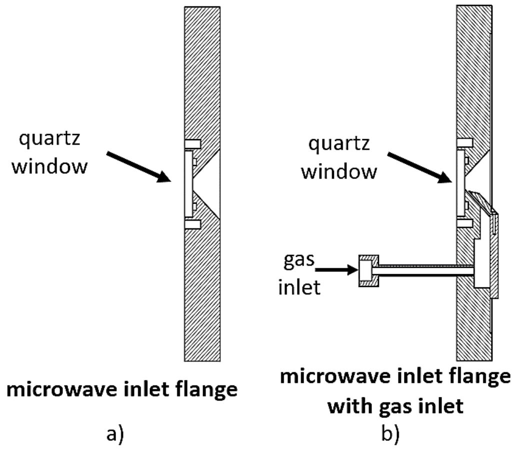

Figure 3.3: Microwave inlet flange designs. a) Simple flange with quartz glass window, and b) similar flange as [a)] with gas introduction inlet.

3.3 Results and discussion

3.3.1 Ignition and extinction power

In Figure 3.4, the ignition and extinction powers as functions of gas pressure in the three different magnetic field geometries are shown. The microwave power was slowly increased until a stable discharge is initiated to record the ignition microwave power at the corresponding Ar pressure condition. When only the magnetic field from the field coils (FC) are present, ignition occurs at 330 W in the high-pressure range at 15 A current on FC equivalent to a maximum field of 430 G at the quartz window. The required power remains constant down to 3 Pa pressure before it starts to increase exponentially up to 1200 W at 1.3 Pa. When the Nd-Fe permanent magnets (PM) are installed in the microwave inlet region, they provide a maximum magnetic field flux of 480 G at the quartz glass surface. With only the PM inducing the magnetic field, the minimum microwave power required to commence a discharge is about 480 W and the power remains constant down to 1.5 Pa. A dip in the ignition power plot occurs at 0.7-0.3 Pa only to increase again up to 900 W at 150 mPa. When the fields from the permanent magnets and the coils are combined to achieve ECR condition near the inlet of the quartz microwave inlet region, ignition occurs around 190 W at high pressure and slowly increases only up to 430 W even further down to pressures less than 5 mPa. At the lowest observable pressure, when the plasma glow does not propagate across the chamber and is limited at the surface of the quartz glass, the plot is terminated. The extinction power, or the minimum power required to sustain the plasma is 240 W with coils, 188 W with magnets and only 90 W at ECR. The extinction power remains constant for each of the conditions above and is represented by the three horizontal lines in Figure 3.4.

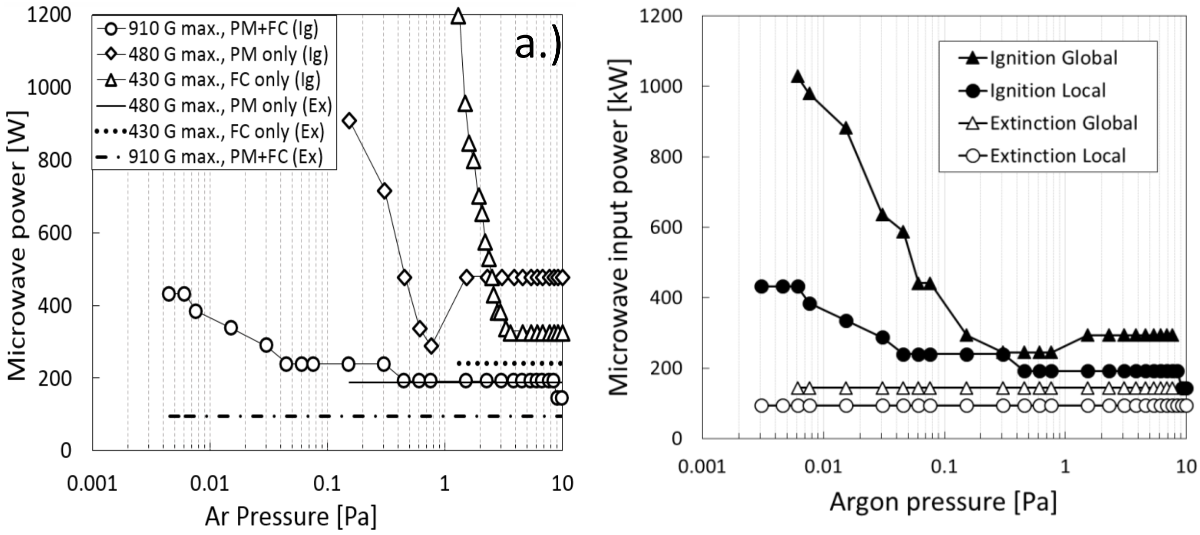

Figure 3.4 a.) Ignition (Ig) and extinction (Ex) powers at varying Ar pressure from different field geometries, namely, field coils (FC), permanent magnets (PM), and combination (PM+FC), b.) and comparison between the different gas introduction

The dependence of the ignition and extinction powers to the strength of the combined fields below 875 G is illustrated in Figure 3.5. The DC source of the coils was controlled to set the maximum field less than 875 G. At 4 A, the total field at the vacuum side of the quartz window surface is 600 G. The ignition power profile follows a similar behavior as when only the permanent magnets are present. This trend continues up to 12 A

(820 G max.) with improved ignition towards the lower pressure range. A dip in the 0.3-0.7 Pa range is also present with a significant increase towards lower pressure. Close to the ECR condition at B = 860 G, there is a considerable improvement in ignition towards lower pressure down to 30 mPa at only 670 W. The extinction power remains constant at 188 W in all of the field intensities below ECR and is also shown in Fig. 3.5.

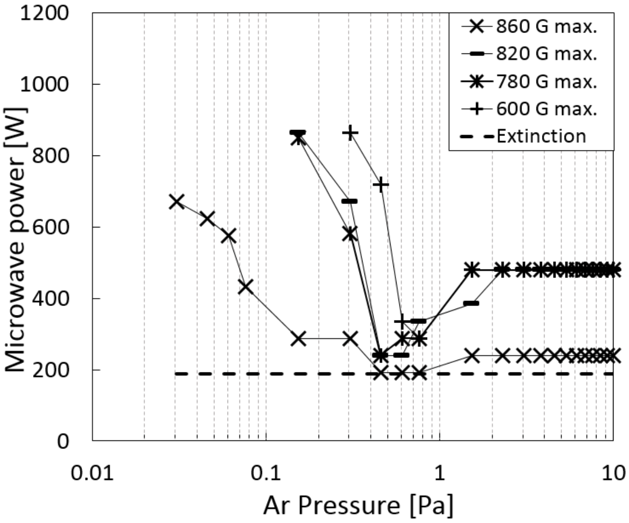

Figure 3.5: Ignition and extinction powers at varying Ar pressure relative to field strength.

From the low pressure region in sub-ECR condition involving permanent magnets, a decrease in the ignition power as the pressure is increased accounts for the decrease in the particle's mean free path inside the chamber as more gas is introduced into the system. As such, an increase in collision frequency promotes more efficient ionization until a minimum ignition power is attained at 0.4 – 0.7 Pa. At pressure greater than at the minimum breakdown, the ignition power is higher but remains invariable. At this point, the electron temperature decreases due to further increase in collision frequency.

Popov et al. [6] observed in their 2.45 GHz microwave plasma device that a reduction in the minimum ignition power occurs when the magnetic flux density is set to be greater than 430 G to which they attribute to the transition from an underdense plasma mode below 430 G to overdense plasma mode at 430-440 G. It is argued that the transition arise from the abrupt increase of the microwave power absorption in the resonance on the second gyrotron harmonic, $\omega=2\omega_{ce}$ [7, 8]. The observed transition to lower power with respect to the flux density corresponds to the same range of minimum power occurrence observed from $B>430$ G. The dip starting from B>430 G manifests this transition towards the minimum power at 188 W in ECR.

3.3.2 Pressure dependence of plasma density

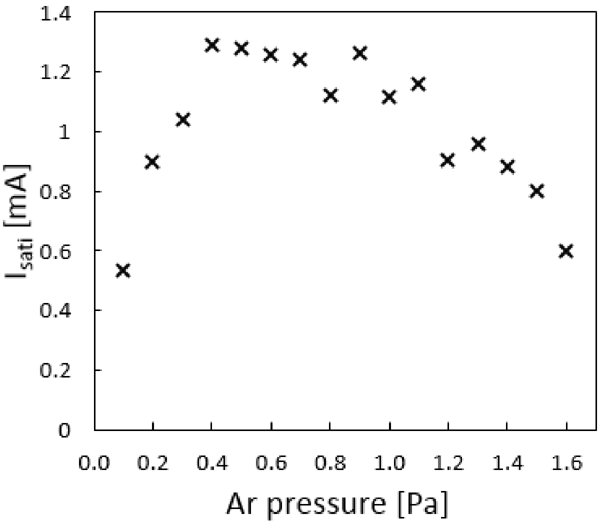

Figure 3.6: Ion saturation current (I_{sati}) at varying pressure along the vacuum chamber's central axis.

Langmuir probe measurement obtained at the center of the chamber at x=0, y=0, around 17.5 cm from the quartz window surface along the plasma downstream, provides the ion saturation current, I_{sati}, of the Ar plasma observed at -75 V probe bias. Fig.3 6 shows the plot of I_{sati} relative to Ar gas pressure at fixed 1 kW microwave power. The current is highest at 0.4-0.9 Pa pressure range and decreases beyond this range in both direction. An estimate of the ionization mean free path, $\boldsymbol{\lambda}_{mfp}$, reveals the behavior of I_{sati} relative to gas pressure. The mean free path is the inverse of the product of cross section, $\boldsymbol{\sigma}$, and number density, n, or $\lambda_{mfp}=1/\sigma n$. At 0.5 Pa gas pressure, n for argon is around $1.33 \times 10^{14} \mathrm{cm}^{-3}$ while an approximate value of the ionization cross section $\sigma = 2.5 \times 10^{-16} \mathrm{cm}^2$ from AMDIS database [9] for a reaction [Ar + e → Ar^+ +2e] is used. From here, $\boldsymbol{\lambda}_{mfp}$ is around 30 cm and is comparable to the device dimension. The total distance from the quartz glass surface to the opposite chamber wall is around 30.5 cm. At lower pressure, particles diffuse towards the chamber wall while recombination is favored at higher pressure.

3.3.3 Sheet plasma profile dependence on magnetic field

A movable stage allows for a 50 mm range of linear vertical motion of the probe tip along the x-axis to determine the axial profile of the plasma. Langmuir probe scans were performed along the plasma width at 3 mm distance for each scan. Ion saturation currents (I_{sati}), electron temperatures (T_{e}), and electron densities (n_{e}) were derived from the I-V curve and are plotted in Fig. 3.7. Density distribution of the plasma particles and electron temperature depict the sheet plasma thickness and its behavior in the presence of varying linear magnetic field. The plasma was maintained by 2 kW microwave power at 0.5 Pa while field measurements were obtained at the center of the chamber along the probe scan direction at $x = 0$. Starting at lower field (13 A equivalent to 265 G), the axial profiles of the I_{sati} and n_{e} behave similarly and form a gradual gradient peaking at $x = 0$. An increase in the field strength (14 G for every 1 A increase in coil current) slightly elevates the gradient while maintaining the same axial profile. When the current is set at 15 A, the field at $x = 0$ is 293 G while an ECR condition is achieved near the quartz window. The ion saturation and electron density magnitudes form steeper gradient with greater magnitude increase along the center of the plasma sheet achieving electron density ~10^{18} m^{-3}. The electron temperature axial profile shows high energy electrons populating the center of the plasma. The field strength did not affect the electron temperature largely because the present treatment to determine the electron temperature uses the low temperature Maxwell component. The ECR condition enhanced the ionization while the increase of magnetic field in sub-ECR condition did not improve sheet plasma thickness.

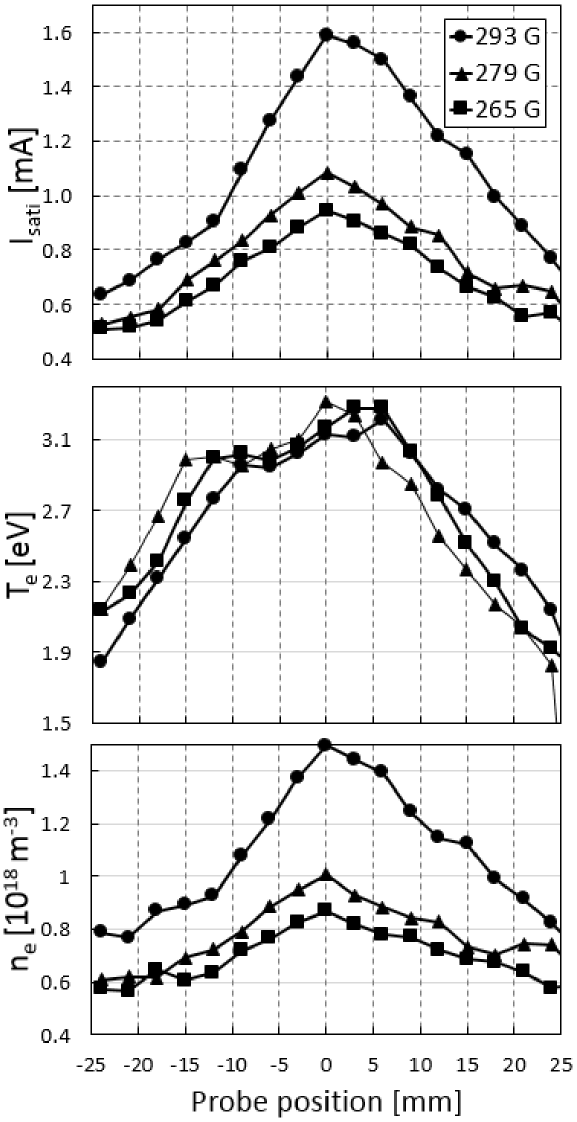

Figure 3.7: Axial profiles of ion saturation current (I_{sati}), electron temperature (T_e) and of electron density (n_e) relative to magnetic field strength along the *x*-axis. The indicated fields were measured at position $x = 0$.

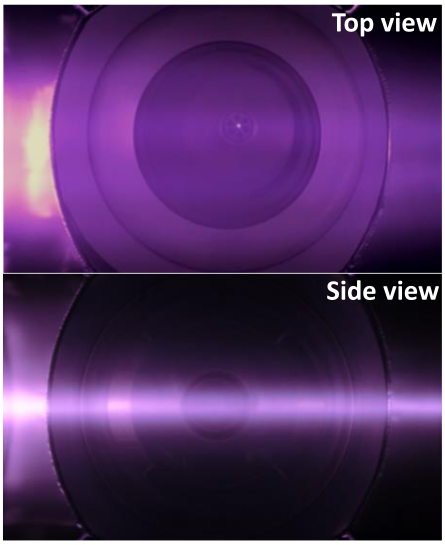

Figure 3.8: Images of the sheet plasma illustrating the sheet plasma when viewed from the top (Top view) and the sheet thickness along the horizontal center of the chamber viewed on its side (Side view).

Previously reported sheet plasma thicknesses were defined in terms of ion Larmor radius [10, 11] where the sheet thickness is described as approximately twice the mean ion Larmor radius. Gyrating ions move relative to guiding centers that lie in the vicinity of the sheet plasma midplane. Taking the condition at a pressure of 0.5 Pa and magnetic flux density B=293 G, the ion Larmor radius, r_i, is approximately 7 mm when the ion temperature is considered to be around 0.1 eV. In the meantime, r_i can be 38 mm if we assume r_i is determined from ion acoustic velocity for 3 eV electron temperature. When compared to the half width half maximum of the plot of the radial profile of ion saturation current, the plasma thickness is around 34 mm. Figure 3.8 shows the sheet plasma at the same condition when viewed from the top (Top view) and on its side (Side view). The second image reveals the plasma thickness based from the observed plasma glow along the midplane. As reference, the circular profile at the center of the image has a 37 mm diameter. This implies that the plasma has a thickness less than this value which is comparable to the estimate of its full width half maximum value at around 34 mm. Clearly, the observed plasma thickness is less than twice the expected plasma thickness when compared with the calculated ion Larmor radius.

3.3.4 Sheet plasma profile in the presence of varying magnetic field

The effect of the applied magnetic field on the plasma profile is derived from the collected *I-V* trace for a 1.0 kW plasma discharge. The plasma profile from the plasma parameters, namely, ion saturation current (I_{sati}), electron temperature (T_e), electron density (n_e), floating potential (V_F) and plasma potential (V_{plasma}), are derived from the I-V trace.

Figure 3.9 shows the ion saturation current (I_{sati}) profile for varied coil current. It increases as the coil current is increased up to 15 A. The profile is maximum above the plasma center. The upper half of the plasma sheet registered higher I_{sati}. As the magnetic field is increased, the gradient profile becomes more evident especially at ECR.

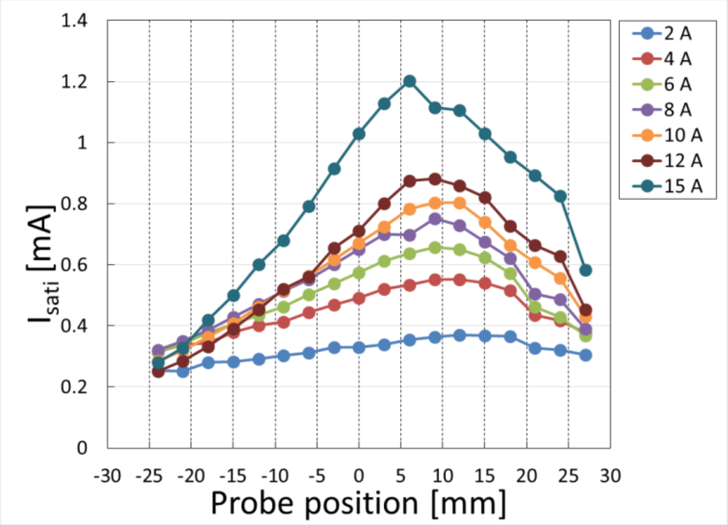

Figure 3.9: Ion saturation current (I_{sati}) axial profile of the plasma at varying magnetic coil current.

In Figure 3.10, the plot of the electron temperature profile is shown for different coil current along the central vertical axis. Near the center, T_e increases due to the increasing magnetic field. The transitions at probe positions -12 mm and 18 mm where the electron temperature is almost constant. As the probe tip moves away from the center, the T_e decreases. In addition, beyond the transition point, T_e profile with increasing coil current reverses, meaning, electrons have lower energy at higher coil current. As the magnetic field strength is increased, the confinement effect for higher energy electrons manifests more clearly as evident from the saturated region between -9 mm to 21 mm. The electrons have, generally, lower energies than the electrons at higher field flux density.

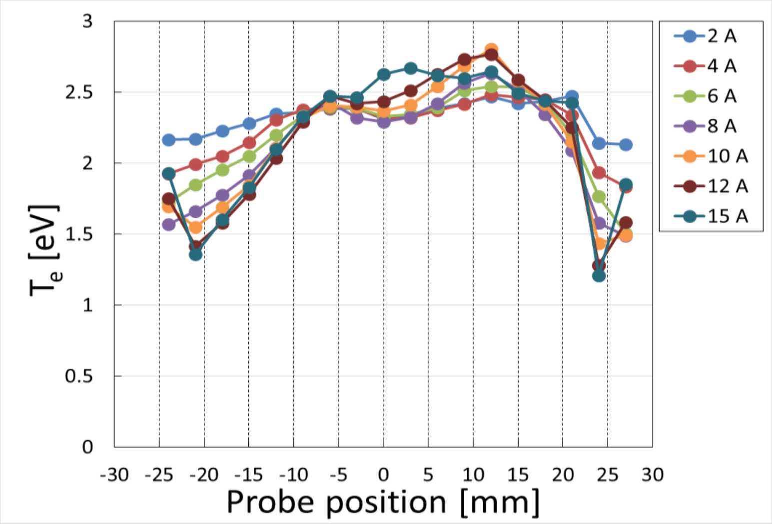

Figure 3.10: Electron temperature (T_e) axial profile of the plasma at varying magnetic coil current.

The axial profile of the sheet plasma relative to electron density is shown in Figure 3.11. It is also maximum at around 6 mm and decreases on both direction similar to I_{sati} profile. At 15 A, the profile shows a significant increase, corresponding to the presence of an ECR condition.

The floating potential signifies the zero-current value along the probe tip. The plot in Figure 3.12 shows the trendline at varying coil current. Moving upward, the floating potential minimizes at 12 mm and slightly increases again along the top portion of the sheet thickness. The minimum corresponds to the region with the energetic electrons corresponding to faster arrival of the electrons as the voltage is swept from negative to positive.

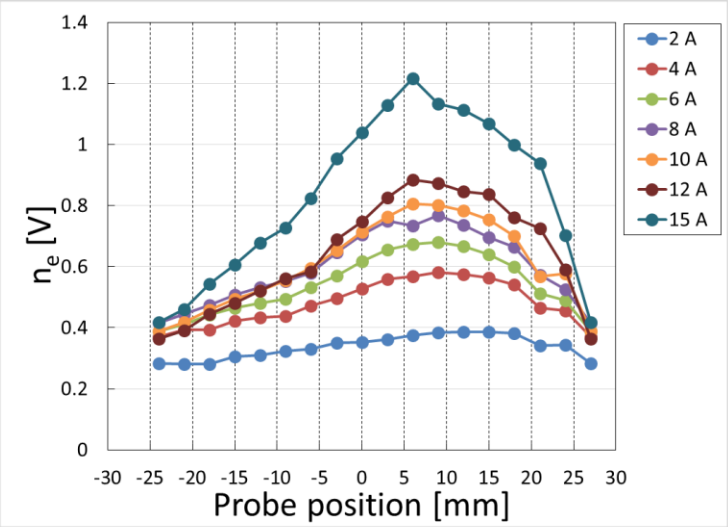

Figure 3.11: Electron density (n_e) axial profile of the plasma at varying magnetic coil current.

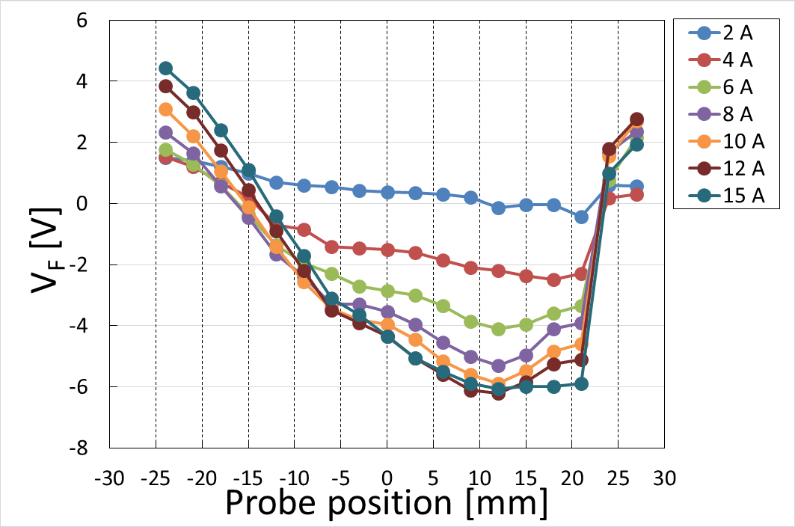

Figure 3.12: Floating potential (V_F) axial profile of the plasma at varying magnetic coil current.

The plot of the plasma potential profile is shown in Figure 3.13. At periphery of the plasma thickness, the plasma potential is very positive. This corresponds to higher presence of positive plasma species. As we move towards the center, the plasma potential becomes almost zero especially at high coil current. At maximum coil current, the V*plasma* minimizes at the center. From the lower coil current range, the plasma potential increases gradually to higher current. After 8 A, the plasma potential increases by almost a 2 V magnitude.

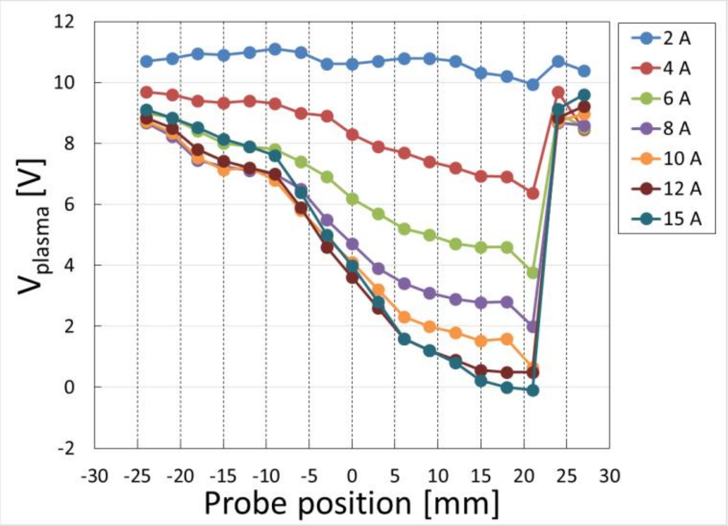

Figure 3.13: Plasma potential (V_{plasma}) axial profile of the plasma at varying magnetic coil current.

3.3.5 Pressure dependence of sheet plasma profile

The pressure of the sheet plasma can be operated at three orders of magnitude range. To attain optimized condition, it is important to determine the behavior of the plasma across a stable pressure range. The plasma performance of the device was analyzed in terms of the I_{sati} at different argon pressures. Figure 3.14 shows the plasma from the side viewport at varying gas pressure at 1.0 kW while the coil current is set at 15 A. Plasma cathode is on the left side of the images. At 0.1 Pa, the sheet appears more dispersed but transforms to a thinner sheet towards the higher pressure range. At 1.0 Pa, an early onset of plasma detachment can be observed on the right side.

In Figure 3.15, a plot of the I_{sati} taken from the vertical axis of the center of the chamber at different gas pressure The plot shows a twin peak, which is typical at this input power. A dip at the center of the sheet was present. A dip occurs at zero. 0.5 Pa shows the highest I_{sati} value at the center.

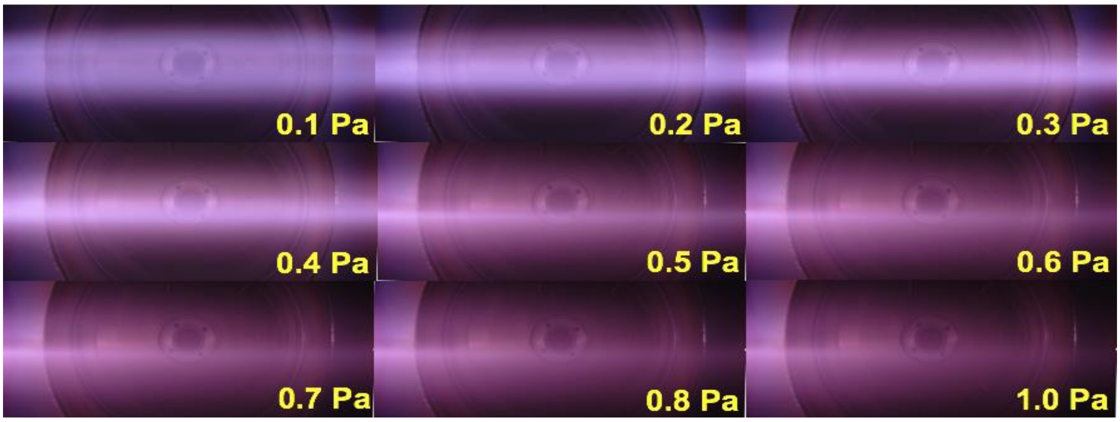

Figure 3.14: Images of the Ar sheet plasma taken from the side viewport at varying pressure.

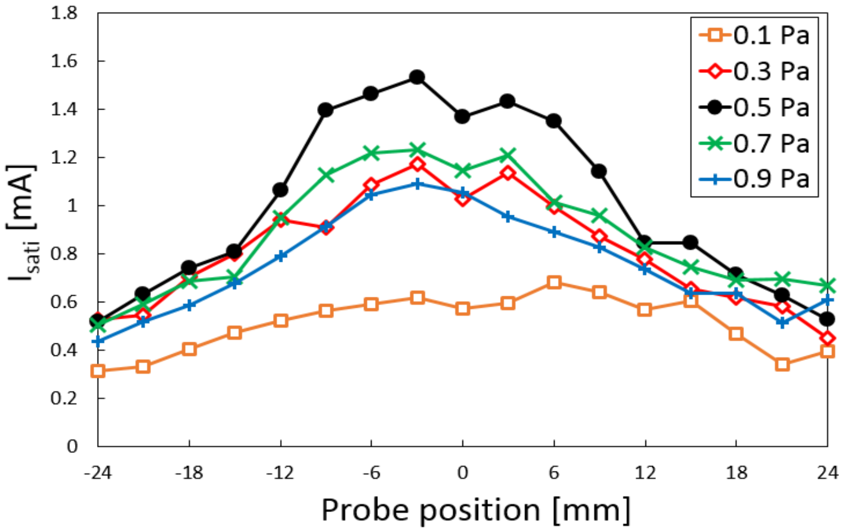

Figure 3.15: Ion saturation current (I_{sati})profile of the sheet plasma thickness at varying pressure.

3.3.6 Microwave power dependence of sheet plasma profile

Ion saturation current measured across the sheet plasma was taken during operation at different microwave input powers and is shown in Figure 3.16. The dip initially observed at the center at 1 kW disappeared at higher power. At higher power, the centers were replaced by higher I_{sati} values. Photos of the sheet plasma is also shown in Figure 3.15. The intensity of the plasma glow increased at higher power.

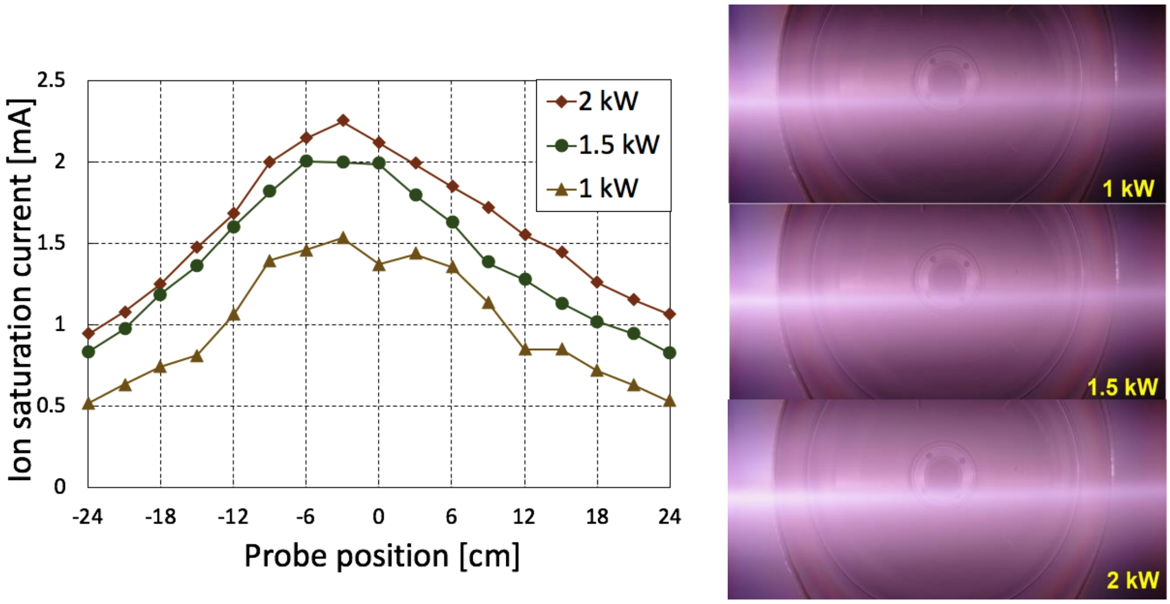

Figure 3.16: Ion saturation current (I_{sati})profile of the sheet plasma thickness at varying pressure.

3.3.7 Comparison of field coil configuration

The applied current in the magnetic field coils generates a linear magnetic field that is directed towards the opposite of the microwave window. Reversing the polarity of the coil reverses the direction of the applied field. In Figure 3.16, a plot of the ion saturation current at normal coil polarity and in the case when the current is reversed. The appearance of the plasmas are also shown. The reverse polarity resulted in lower I_{sati} across the sheet thickness. It also remained almost constant. The image shows a thinner sheet produced along the center. The intensity appears intense but could probably due to the integration of the brightness along the viewing line.

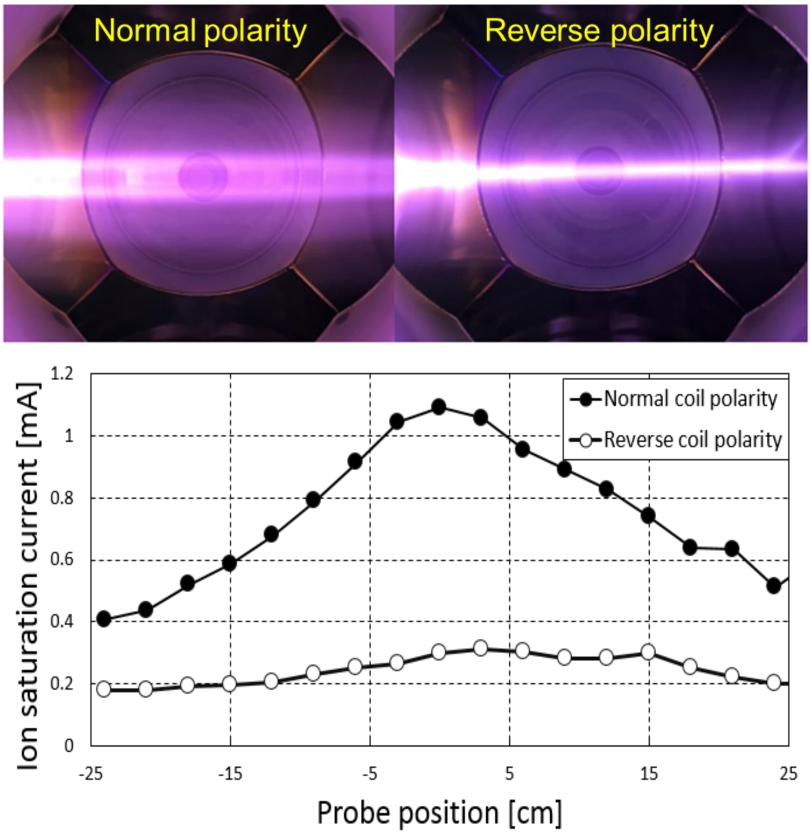

Figure 3.17: Comparison of the plasma at different coil polarities.

3.4 Conclusion

A new sheet plasma device employing a combination of field coils and permanent magnets has been designed and operated. The design includes a gas feed system that cools the quartz window surface allowing plasma operation at microwave power up 3 kW without damaging the quartz glass microwave inlet structure. The field strength raises the plasma density while ECR condition significantly enhances plasma production to attain electron density to 10^{18} m^{-3} range. The electron temperature of the bulk plasma remains independent of the magnetic field strength.

References

[1] M. Yoshida, K. Kajinishi, IEEE Transactions on Plasma Science **31**, 40-48 (2003).

[2] N. Morishita, S. Ishii, Y. Kato, F. Tani, Y. Koizumi, M. Sunagawa, Proceedings of 11th International Conference on Ion Implantation Technology **2**, 752-755 (1998).

[3] V.R. Noguera, H.J. Ramos, Thin Solid Films **506-507**, 613 (2006).

[4] H.J. Ramos, K. Doi, M.S. Fernandez, G.M. Malapit, M. Sasao, M.M.S. Villamayor, M. Wada, JPS Conf. Proc. **1**, 015060 (2014).

[5] J.W. Davis, D.E. Driemeyer, J.R. Haines, R.T. McGrath, J. Nucl. Mater. **212-215**, 1353(1994).

[6] O.A. Popov, S. Y. Shapoval, D.Y. Yoder Jr., Plasma Sources Sci. Technol. **1**, 7 (1992).

[7] T. Stix, *Waves in Plasmas* (New York: Springer-Verlag, 1992) p. 270.

[8] J. Datlov , J. Teichman , F, Zacek, Phys. Lett. **17**, 30 (1965).

[9] AMDIS ionization database, NIFS database, Japan National Institute of Fusion Science.

[10] K. Sukani, K. Nanri, T. Noguchi, E. Yabe, K. Takayama, Nucl Instrum Methods Phys Res B **111**, 151 (1996).

[11] Y. Okuno, H. Ishikura, H. Fujita, Rev. Sci. Instrum. **63** (7), No. 7, 3725-3728 (1992).

Chapter 4

Local Gas Injection Type Dielectric Window

The emission lines of hydrogen plasma are investigated to study the effect of using the gas feed as cooling mechanism for the microwave inlet region in a sheet plasma device. The spectra were observed for different gas introduction modes with spatial dependence across the quartz window region. Observation of molecular assisted recombination (MAR) when gas is introduced in the quartz surface in a dominantly ionizing plasma condition determines effectivity of the cooling mechanism.

4.1 Introduction

Molecular assisted recombination (MAR), as a mechanism for heat flux reduction, was experimentally observed in plasma divertor condition from hydrogen gas puffing to helium plasma [1]. In most studies, MAR is usually observed in the edge of magnetic confinement devices. Observation of MAR in the ionizing region to explain heat reduction in the microwave window was conducted. In the cathode region, heat is generated ,sometimes excessively, due to plasma confinement effects brought by magnetic-mirror which occur at maximum in this region.

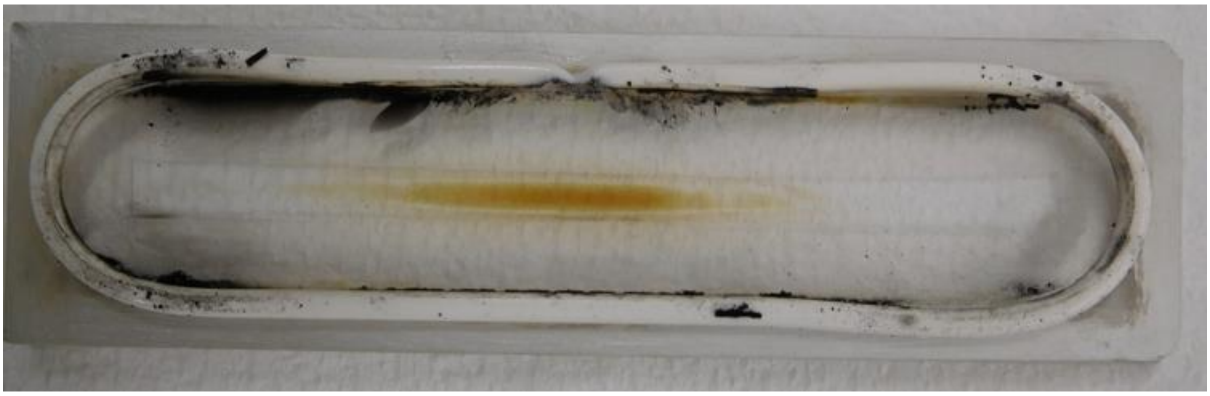

Figure 4.1: Image of the burnt quartz window and rubber O-ring seal.

In the present set-up the microwave inlet region was observed to generate excessive heat when operated at higher microwave input power. In fact, in the first generation design of the microwave window flange, the high temperature rubber O-ring and the quartz window were damaged from high power operation beyond 1.5 kW. In excess of heat, a part of the quartz window melted while the rubber O-ring totally burnt up. An image of the quartz window is shown in Figure 4.1 highlighting the vacuum side of the window. It can be seen that the heat concentrated on the rubber O-ring-glass-quartz-interface. Black soot can be observed around the rubber seal in contact with the glass window. Eventually, the pressure of the chamber was not maintained by the vacuum seal and terminated the plasma generation.

4.2 Methodology

Gas is initially introduced into the main chamber through an inlet flange perpendicular to the plasma drift, along the *z*-axis. Plasma is generated, mainly, in the vicinity of the quartz window which creates considerable heating onto the plasma-facing components. The part of the copper waveguide that is parallel to the quartz window is fitted with a water-cooling coil to quench the constant heating plasma is turned on. However, at microwave powers exceeding 1.5 kW, the rubber O-ring burned which melted parts of the quartz glass eventually altering the vacuum condition.

During plasma operation, the microwave input power was maintained at 1.5 kW. The coil current is maintained at 12 A equivalent to a magnetic flux density of 345 G in the microwave inlet region. This time, two permanent magnets were installed.

A planar slit conduit is created by fitting a stainless steel panel parallel on the lower side of the diverging wall of the flange holding the quartz glass window. The small width helps to create a localized high gas pressure reaching the quartz window. This component is intended to help reduce heat flux in the region while also providing steady stream of the gas to be ionized. Initially, a power higher than 1.5 kW introduces considerable heating which burns the carbonless rubber O-ring between the stainless steel flange and the quartz glass. The heating-up magnifies at lower range of the plasma operation pressure. As such, a similar configuration was applied to simulate the same condition.

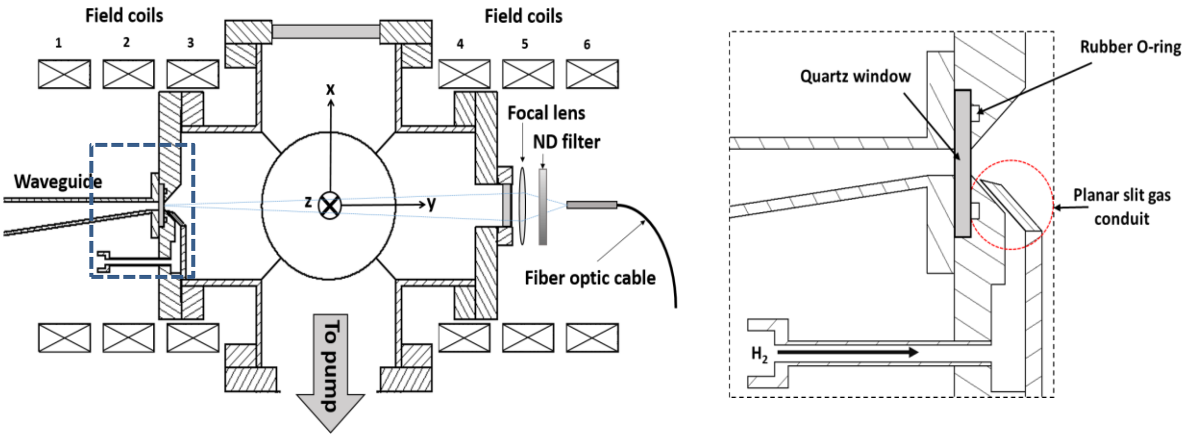

Figure 4.2: Schematic diagram of the experimental set-up.

Hydrogen gas was utilized as the neutral gas. In many known studies, the observation of heat flux reduction via molecular assisted recombination was done in hydrogen plasma. It was determined that the increase in Fulcher band emission signifies recombination processes that are associated to maintaining heat flux in plasma divertors and plasma device anodes.

An *Ocean Optics 2000+* optical emission spectrometer coupled to an optical fiber records the emission spectra of the plasma in the visible region. It has a wavelength resolution of 0.38 nm. The spectra is collected from the viewport confronting the vacuum side of the quartz glass window. A 50 mm focal lens was used to focus the plasma emission reaching the optical fiber tip. In addition, a neutral density filter was also employed to limit the emission intensity reaching the probe tip, which has high saturation due to the focused light rays.

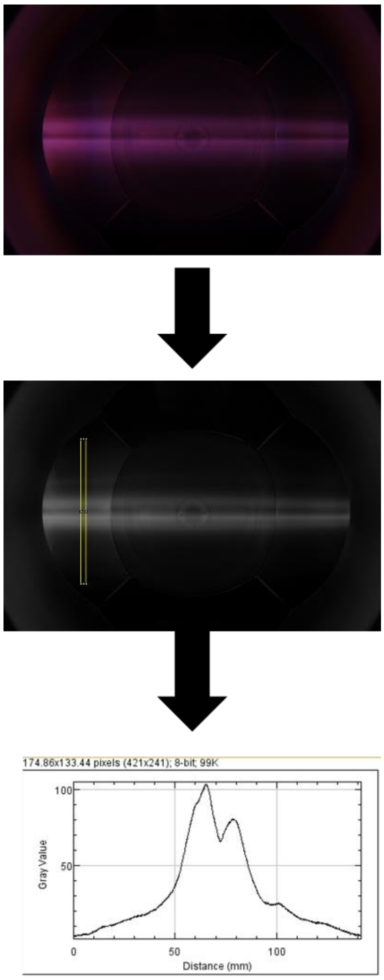

Figure 4.3: Diagram of plasma image processing of converting the image to a grayscale and then to a numerical value of pixel brightness.

Plasma images were captured by a Pentax K-7 digital camera. The images were taken from the side, top and on the terminal flange confronting the microwave window. The images were taken at fixed aperture size, shutter speed, ISO and focal length for each batch of data. To derive more standard information on the acquired images, they were processed in *ImageJ* image processor. First, the images were converted to a stack image for much faster processing. Then, they are converted to an 8-bit file which turn the images into a grayscale. A feature in the photos with a known dimension was measured to be used as calibration constant for the conversion of pixel to a physical dimension of the image. By this point the pixel brightness would be converted to a numerical value from 0 to 255 to correspond to the relative brightness from low to high. The RGB images are converted to grayscale using the formula, Gray=(0.299red + 0.587green + 0.114blue), derived from YUV color encoding system used in analog TV broadcasting. The values are plotted versus the derived relative size and position.

4.3 Results and discussion

4.3.1 Observation of possible molecular assisted recombination (MAR)

Hydrogen plasma produces visible light emission from neutral excitation of atoms and molecules by electron impact to higher energy level and decay via spontaneous emission. The typical emission spectra of hydrogen plasma is shown in Fig. 4.4. The graph shows strong emission lines from the hydrogen Balmer series as well as the Fulcher band at 600-640 nm. For hydrogen gas, plasma can be sustained down to 4 Pa. The pressure dependence of the emission lines H_α, H_β, and H_γ and the Fulcher-α was investigated. In the cathode region, the emission spectra observed was that of an ionizing plasma wherein strong line of H_α is dominant. In Fig. 4.4, the emission intensity of H_α is shown. An increase in pressure results in a decrease in H_α emission intensities which also corresponds to a decrease in the excitation temperature confirming the reduction of electron temperature at higher pressure due to increased collision events. In general, a similar behavior was observed in both modes. The dependence of the emission intensity of H_α and the intensity ratios of H_β/H_α and H_γ/H_α on pressure for different gas channels is shown in Fig. 4.5. The spectra were obtained in the regions 4 mm above and below the quartz window surface center axis. The maximum intensity of H_α is attained at around 10 Pa. The ratio decreases as the pressure is increased. A bump around 9 Pa also occurs near the gas conduit for the case where gas emanates from it. The H_α intensity abruptly reduces at 4 Pa.

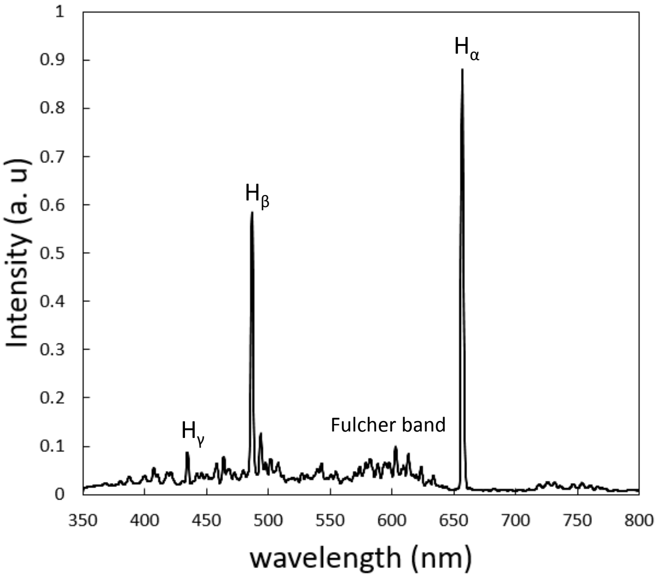

Figure 4.4: Typical emission spectra of hydrogen plasma in a microwave sheet plasma device.

The intensity ratios decrease towards the high pressure. In the planar slit gas mode, a bump in the trend was observed in the lower region of the window at around 9 Pa, corresponding to the maximum of H_γ but did not change largely to the rest of the pressure range. The intensity is lowest near the planar slit conduit with gas introduced through it.

The intensity ratios around 10 Pa are also the highest. An increase in intensity of H_α, $I_{H\alpha}$,indicates MAR.

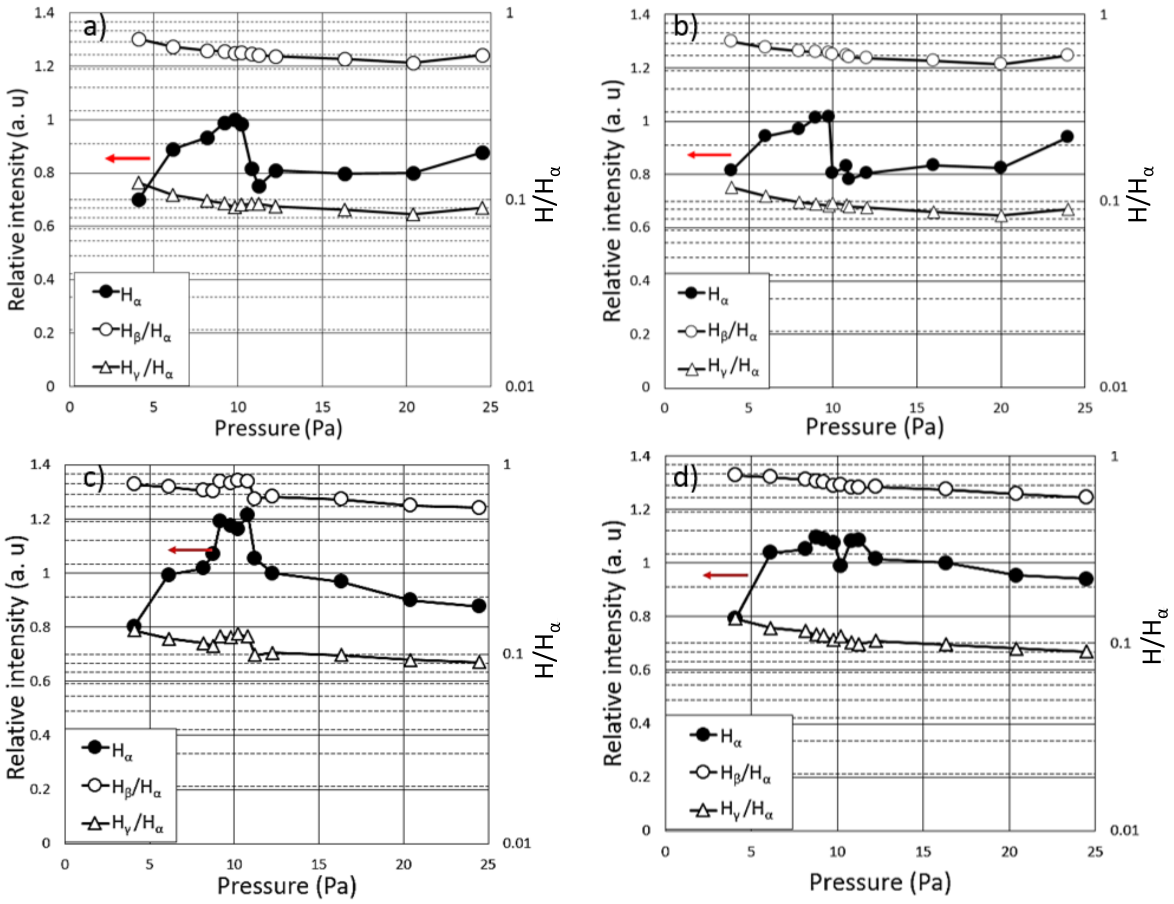

Figure 4.5: Emission intensity of H_α and the semi logarithmic plot of the intensity ratios of H_β/H_α and H_γ/H_α on the planar inlet via a) planar slit gas conduit, b) directly on main chamber and 7 mm above c) via (a)) and d) (b)).

The graphs in Figure 4.6 express the normalized integrated intensity of Fulcher band using the H_α peak for the two gas channels. In general, the slit conduit produces higher Fulcher-α total intensity over the entire gas pressure range which indicates higher recombination of hydrogen species for this gas introduction mode. Although, the utilized method provided limited spectral resolution for the specification of Fulcher-α band lines, this band is identified as molecular hydrogen.

Two regions were considered to observe the spatial dependence of the plasma species from the conduit. The region of the conduit and a spot, 7 mm above it was considered. In Figure 4.6a) and 4.6b), the ratios of the integrated sum of Fulcher-α band and H_α at two positions (in red dots on the left) show a consistent increase as the pressure is increased. A bump in the plots also occurs at around 10 Pa. Near the gas conduit, the ratio is higher when gas emanate from this region than when gas is directly fed in the main chamber but higher intensity ratio is observed on the upper region of the window. Higher ratio of Fulcher band integrated intensity and H_α was observed at the region above the conduit.

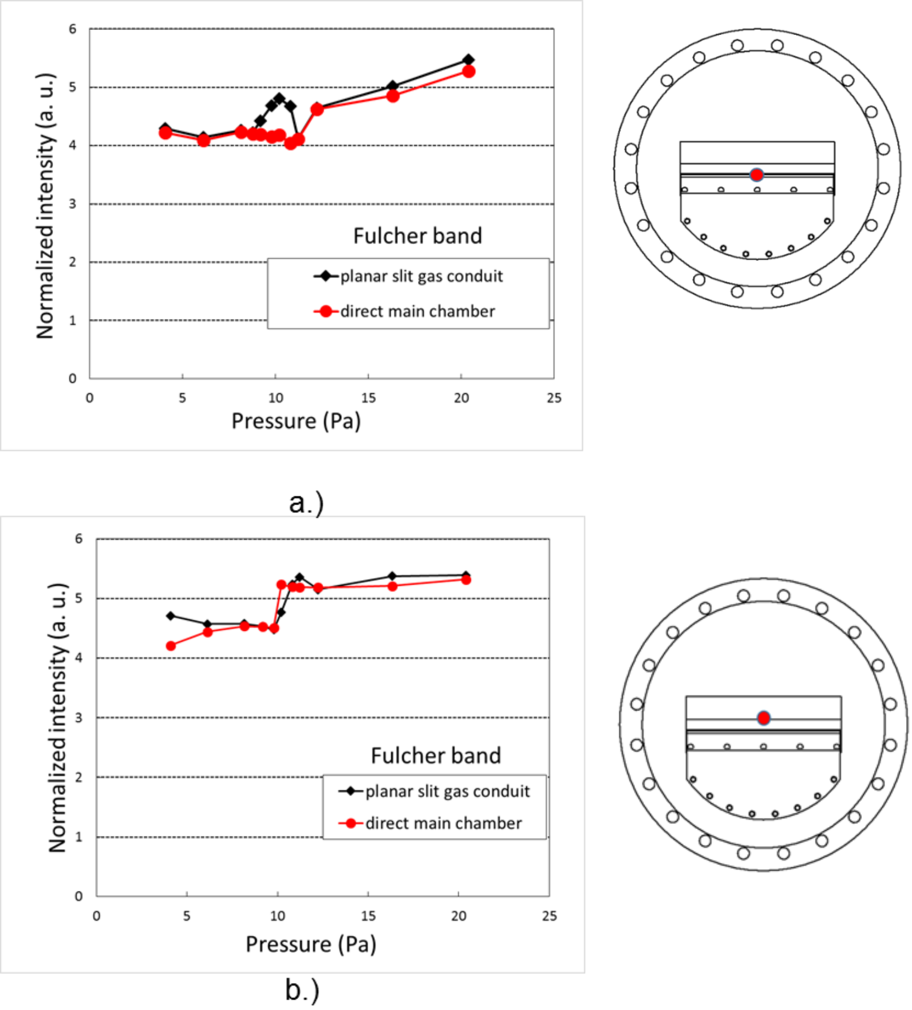

Figure 4.6: Normalized integrated intensity of Fulcher band on the a) planar conduit opening and b) 7 mm above the planar conduit.

4.3.2 Observation of plasma thickness

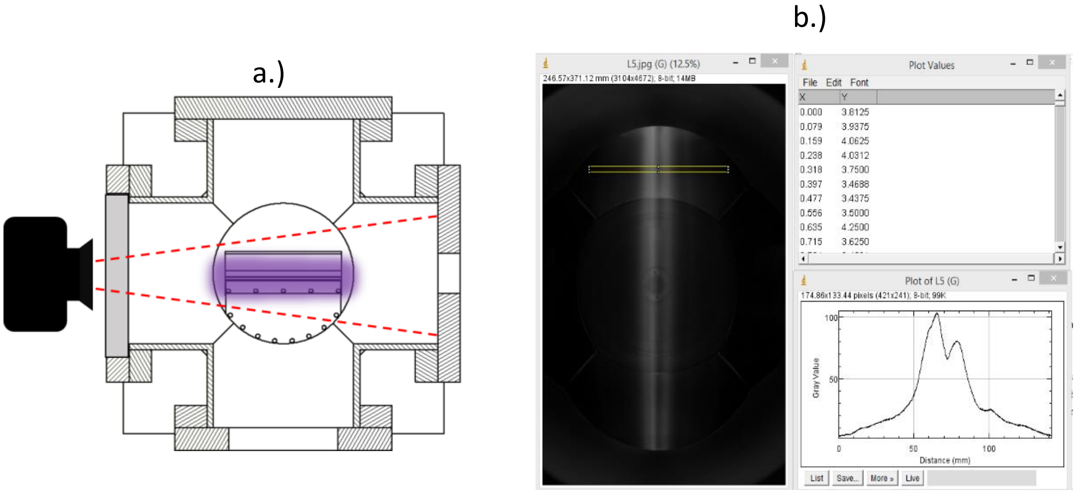

```
X       Y
0.000   3.8125
0.079   3.9375
0.159   4.0625
0.238   4.0312
0.318   3.7500
0.397   3.4688
0.477   3.4375
0.556   3.5000
0.635   4.2500
0.715   3.6250
```

Figure 4.7: a.) Camera position and b.) Sample of the plasma luminous intensity of the captured plasma glow of the plasma viewed on the side of the chamber.

Images of the sheet plasma were taken from the side view port window flange of the chamber, as shown in Figure 4.7a), at varying pressure of hydrogen gas. Moreover, the plasma taken from different gas introduction configurations were observed. The region of interest (ROI) was chosen near the microwave window, as in Figure 4.7b). The width of the chosen ROI was made thin enough to eliminate effects of diffusion after averaging the columns of pixels. Moreover, the width was chosen such that the periphery with less intensity can be compared with that of the emission of the plasma column at the center. The plots of the luminous intensities of the plasma column at varying pressure and gas introduction modes are shown in Figures 4.8 and Figure 4.9. In both modes, the plasma profile shows twin peaks near the center. The intensity increases with respect to pressure. At increasing pressure, the twin peaks merge to form a stronger single peak. Comparing the two modes, the intensities show similar profiles and behavior at increasing pressure. In terms of the relative intensity of both modes, the intensity values were subtracted and is shown in Figure 4.10. The plot confirms the higher emission intensity for the local gas injection mode.

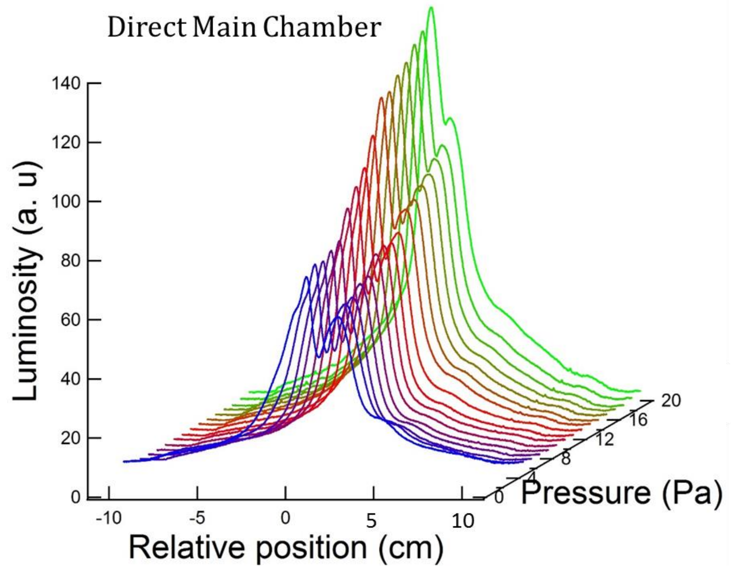

Figure 4.8: Luminous intensity of the observed plasma glow viewed on the side when gas is introduced directly to the main chamber.

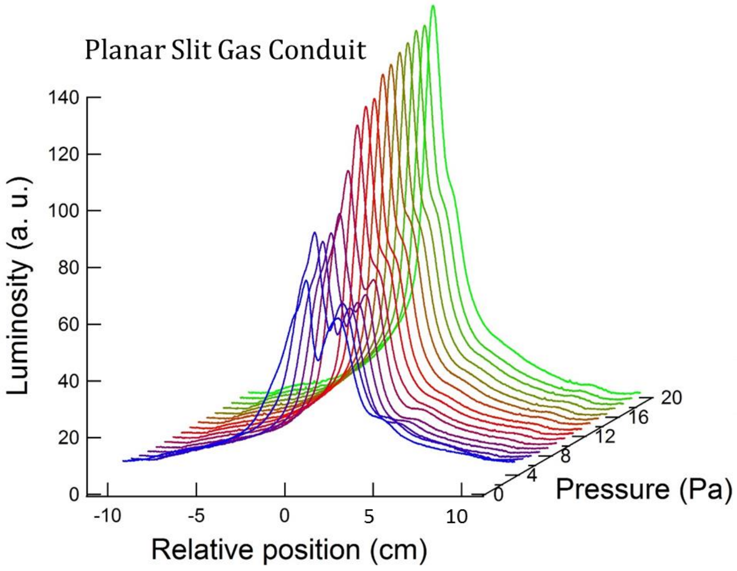

Figure 4.9: Luminous intensity of the observed plasma glow viewed on the side when gas is introduced via the planar slit conduit.

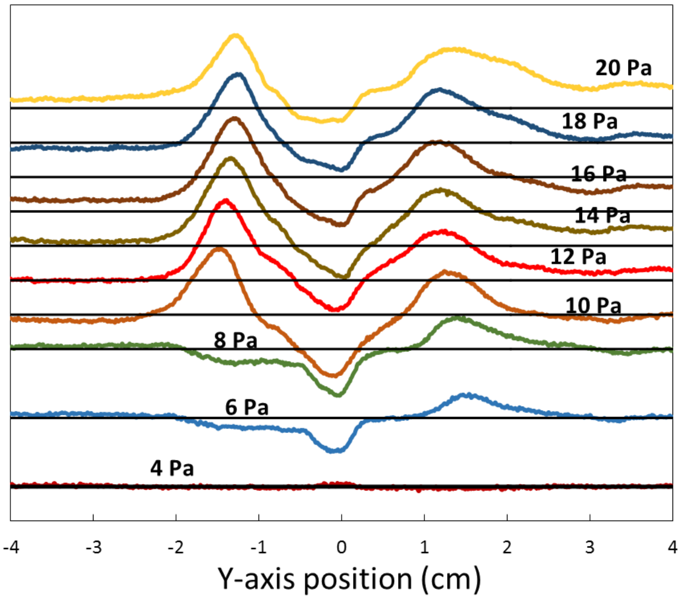

Figure 4.10: Difference in the intensity between direct gas injection and via planar gas conduit.

4.3.3 Observation of microwave window

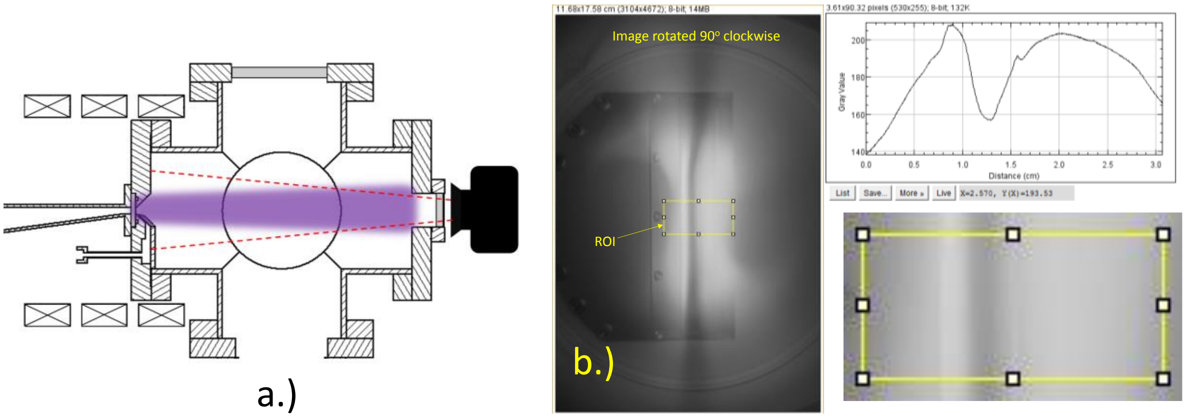

Figure 4.11: a.) Camera position and b.) Sample of the evaluation of luminous intensity of the captured plasma glow in the vicinity of quartz glass window.

Images of the plasma glow are taken from the vicinity similar to the OES set-up. Figures 4.12 show the plotted luminous intensity of the plasma observed when confronting the microwave window when gas is introduced in two different ways. The broken lines indicate positions of the strong intensity peaks corresponding to the edges of the stainless steel window. It also shows the plasma expanding above and below the microwave window edges especially at low pressure range. Meanwhile, the peaks show that the maximum intensity is not symmetric with respect to the determined geometry of the microwave window. Higher intensity was observed on the upper microwave window. It is more likely that the high pressure neutral gas stream from the planar conduit promotes more plasma species trajectories upward, thus producing more glow. At higher pressure, the plasma glow appears to form more symmetrically.

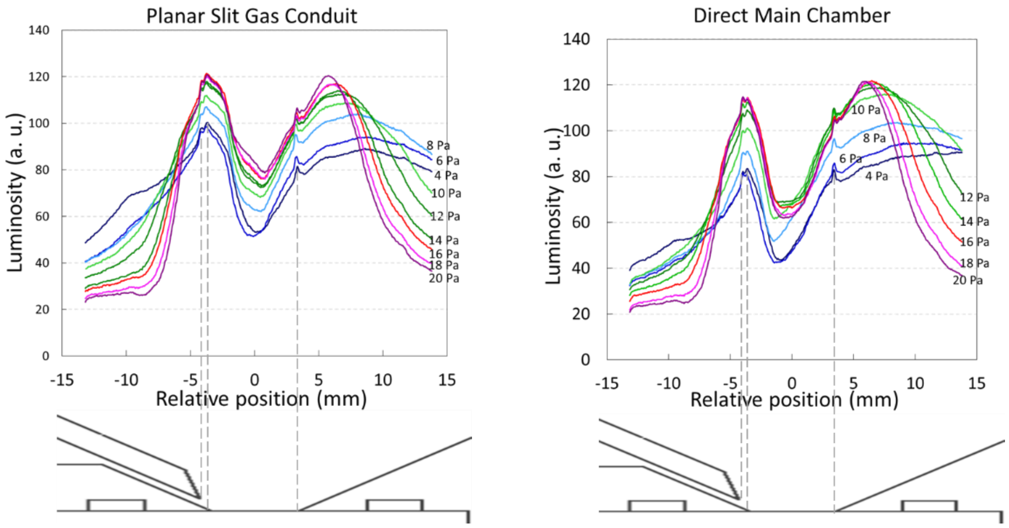

Figure 4.12: Luminous intensity of the observed plasma glow in the microwave window when gas is introduced via the planar slit gas conduit and directly into the main chamber.

The difference in the luminosity based on the intensity values of the plasma images from two gas channel modes was taken to compare the effect of the local gas injection and is shown in Figure 4.13. The plot shows that the luminosity is more intense at the lower part of the window while enhancing the glow at the upper portion for the direct chamber gas injection. Meanwhile, Figure 4.14 shows the total luminous intensity of at varying pressure corresponding to the two gas introduction modes. The total intensity did not change significantly between the two modes suggesting that the discharge remains the same in both gas delivery methods.

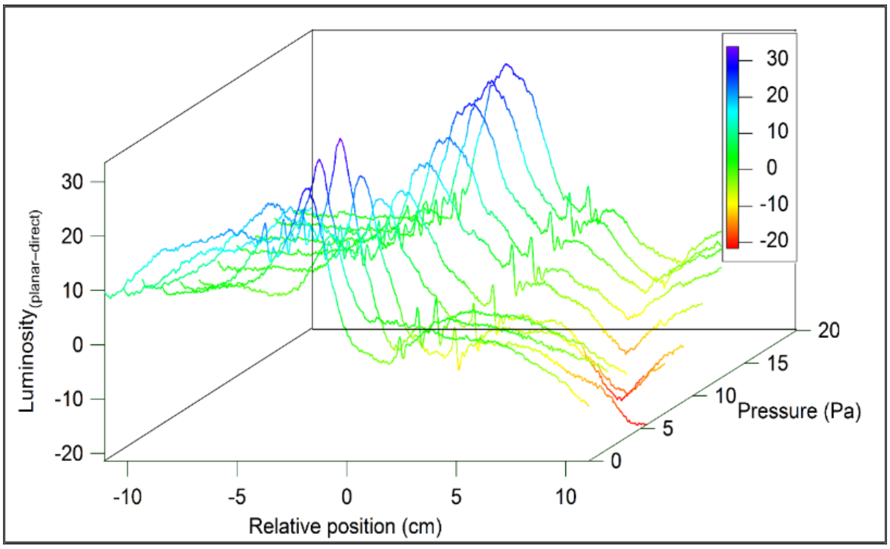

Figure 4.13: Subtracted luminous intensity observed in the microwave window from the two gas modes.

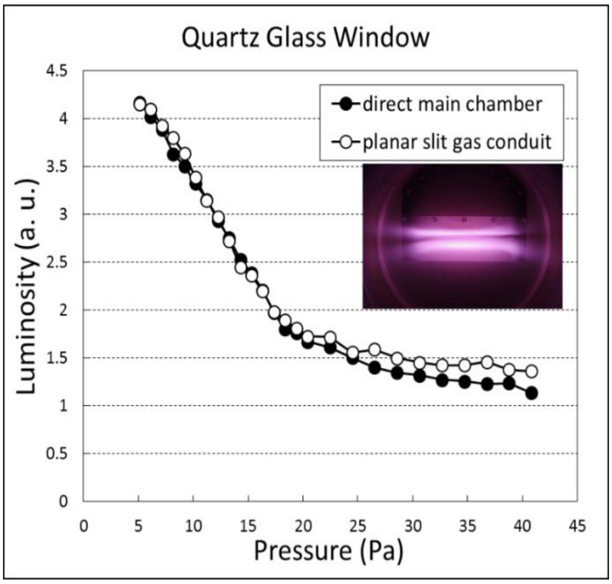

Figure 4.14: Total luminous intensity observed in the microwave window from the two gas modes.

4.3.4 Top view observation of sheet plasma

This time, the sheet plasma was observed from the top of the vacuum chamber to reveal the approximate plasma width as shown in Figure 4..15. Images of the plasma were taken at varying hydrogen gas pressure introduced via the two gas inlet modes: local injection in the quartz glass window and directly onto the main chamber. The two modes were analyzed for their effects on plasma luminous intensity and also to observe the sheet width.

ImageJ software, as shown in Figure 4.15. was again utilized to convert the optical glow recorded by the plasma images to a numerical value ranging from 0 to 255 corresponding to the perceived pixel brightness. A standard measurement was done on the image to determine the relative size of each pixel as well as assign a relative position in the image. In this case, the inner diameter of the chamber was taken as the standard feature. An arbitrary region of interest (ROI) was selected in the image as shown by the yellow box superimposed in the B/W image. The ROI was selected to cover all the bright optical glow and a part of the periphery to determine the approximate plasma width.

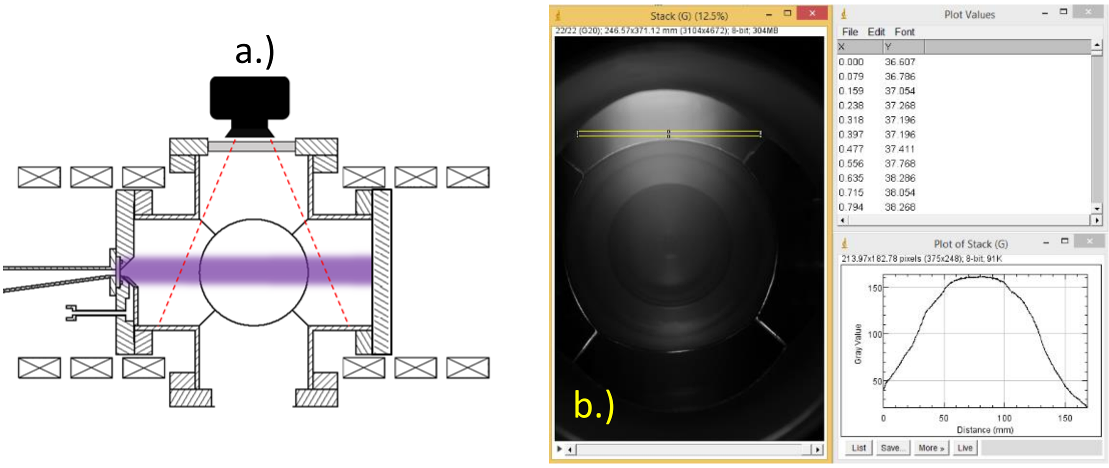

22/22 (G20); 246.57x371.12 mm (3104x4672); 8-bit; 304MB

X	Y
0.000	36.607
0.079	36.786
0.159	37.054
0.238	37.268
0.318	37.196
0.397	37.196
0.477	37.411
0.556	37.768
0.635	38.286
0.715	38.054
0.794	38.268

213.97x182.78 pixels (375x248); 8-bit; 91K

Figure 4.15: a.) Camera position and b.) Sample of the plasma luminous intensity of the captured plasma glow of the plasma viewed on the top of the chamber.

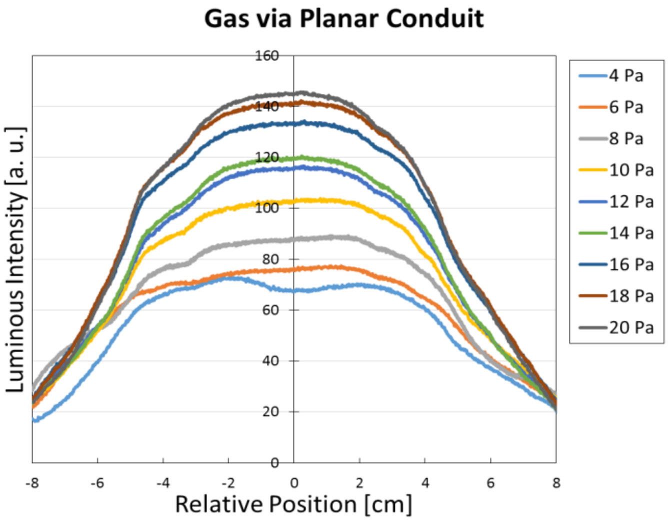

Figure 4.16: Luminous intensity of the observed plasma glow when gas is introduced via the planar slit.

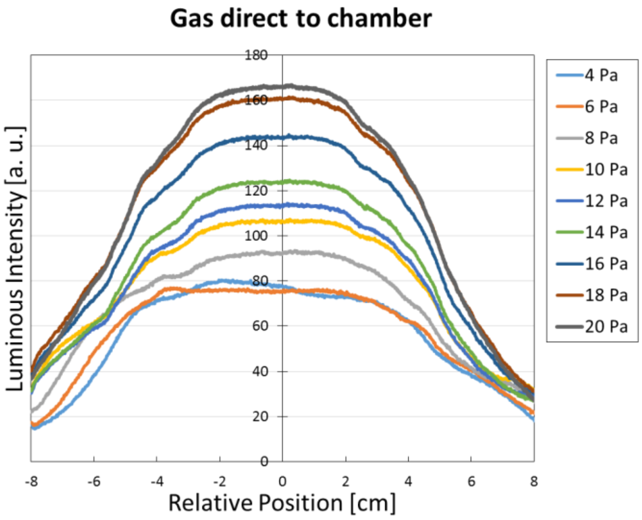

Figure 4.17: Luminous intensity of the observed plasma glow when gas is introduced directly into the main chamber.

Figures 4.17 and Figure 4.18 show the luminous intensities of the plasma at varying pressure via “local gas” and “global gas”. The plot shows that the glow intensifies as the pressure is increased. This time, the plot did not show the saturation pressure but is expected to occur at higher pressure. Relative to the center position, the plasma is uniformly dispersed from the center, except at 4 Pa, with a maximum at this region and decreases towards the chamber periphery. The plasma width can also be determined from the acquired plot. Considering the full-width-half-maximum of the trace, the plasma width is determined to be around 11 cm corresponding to the microwave window width. The pressure slightly increases the plasma width. Comparison of the luminosity intensity of the two modes show that the global gas has higher intensities across the pressure range.

4.4 Conclusion

The effect of installing a local gas conduit in the microwave window region was studied by emission spectroscopy and plasma image analysis. The emission spectra did not hint the effect of cooling from molecular assisted recombination. There is a general increase in emission intensities of the Balmer series for the local injection mode. The acquired plasma images exhibit the plasma profile by observing the plasma optical glow. It was determined that the local gas injection increased the plasma luminosity and improves at higher pressure. Moreover, the plasma exhibit twin sheet which merge at higher pressures. The plasma width is approximated to be around the same size of the microwave window.

References

[1] N Ohno, N Ezumi, S Takamura, S I Krasheninnikov, A Yu, Phys. Rev. Let **40**, 4 (1998).

[2] O. A. Popov. J. Vac. Sci. Technol. *A* **9** (1991): 711.

Chapter 5

Sheet Plasma Excitation by a 2.45 GHz Microwave Power Introduced through a Local Gas Injection Type Dielectric Window

A 2.45 GHz microwave power injected through a quartz glass window produced a stable sheet-shaped plasma with the 11 cm wide and 4 cm high rectangular cross section in a static linear magnetic field. A thin slot gas conduit opened near the surface of the window supplied a discharge gas forming a stream of neutral atoms that intersected perpendicularly the plasma flowing toward the window along the magnetic field. The gas stream caused the change of the luminous intensity distribution of the plasma around the microwave window indicating reduction of the local plasma heat load. The window did not show any damage for a continuous operation of plasma up to 2 kW microwave input power.

5.1 Introduction

Effects due to change in magnetic field intensity to sustain plasmas have been discussed by several researchers [1-6]. Krinberg [1] observed the limit whereby the effect of the applied magnetic field can be used to reduce the size of the plasma column, increase the electron temperature and the average ion charge. Hashemi *et al.* [2] reported that a constriction of the plasma flow was observed with a decrease in plasma jet radius causing an additional Joule heating in a plasma. Woo *et al.* [5] identified the effect of ion temperature anisotropy associated with the induction of a magnetic field.

A system was designed to produce stable sheet-shaped plasma with high density and temperature gradient to be utilized for surface processing application. It was shown that the production of localized electron cyclotron resonance (ECR) region effectively reduced the ignition power and increased the pressure range of stable plasma operation under 1 kW of microwave input power (P_{mw}). This report highlights the performance of the microwave plasma induction structure that should withstand a high-power density heat loading from the produced plasma. The present report on the system includes the transition from sub-ECR to creating a local ECR interaction region. Plasma conditions at the location distant from the plasma production region were measured and analyzed by data obtained from Langmuir probe measurements with optical luminous intensity distributions to observe sensitivity to magnetic field variation. The observation was performed in the region of minimum magnetic flux density, B, in the axial direction of the magnetized plasma. Such observation of plasma in a similar field configuration was performed by Tarvainen *et al.* [7] who found increasing periodic instabilities with increasing magnetic field strength. There are several modifications from the original system: a local magnetic field structure produced by combination of a linear magnetic field and permanent magnets, and neutral gas flow injected to cover the vacuum side surface of the microwave window.

5.2 Experimental setup

The main part of the locally magnetized ECR sheet plasma device is depicted in Fig. 5.1. The main chamber is composed of a stainless steel six-way crosses flange that is 33 cm long and 15 cm in diameter. A dry scroll pump coupled to a 260 ℓ/s turbomolecular pump evacuates the chamber down to <5×10^{-5} Pa.

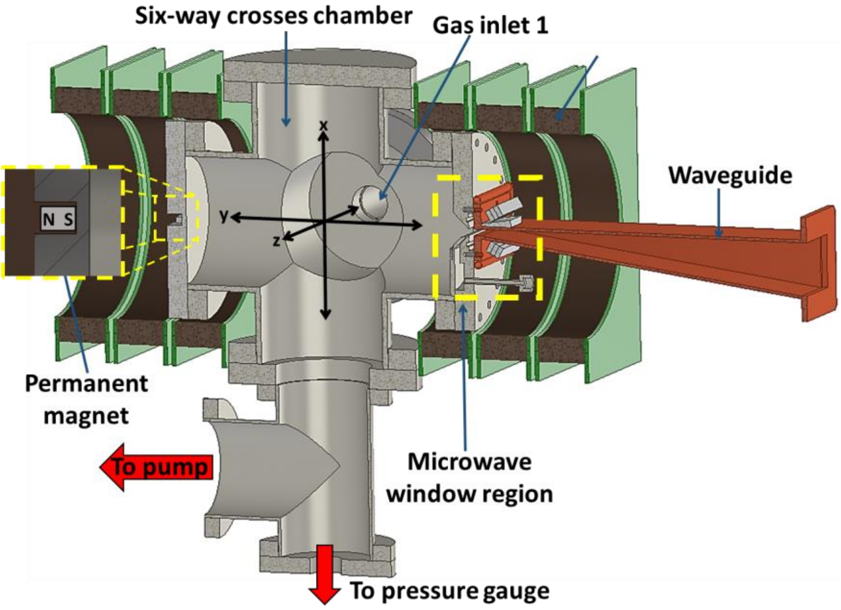

Figure 5.1: Schematic diagram of the sheet plasma

A detailed schematic of the microwave window region is shown in Fig. 2. A 2.45 GHz microwave source can supply up to 3 kW of input power delivered by a tapered copper waveguide through a 7 mm by 110 mm window. A 5 mm thick quartz glass seals the vacuum while transmitting microwave power exposed to the plasma. The window maintains vacuum with a high temperature rubber O-ring, while a silicon rubber framed in copper sheet protects the quartz glass from any damage when in contact with the water-cooled waveguide flange. The water-cooled waveguide flange is attached to the main flange of the plasma chamber to reduce the local heating around the plasma excitation region.

A 1.5 mm by 110 mm slit shape gas conduit directs discharge gas to the vacuum side of the quartz glass to assist further cooling of the cathode region. In Fig. 5.2, red arrows, generated using Flowsquare 4.0 software, illustrate the flow of gas from the gas inlet to the planar slit and exiting towards the quartz window surface where a localized high pressure is created by the stream of gas. Continuous stable operation was achieved up to 2 kW P_{mw} for at least one hour without overheating the device. There is also another gas inlet port installed to feed the discharge gas into the central region of the plasma chamber. The location is indicated in Fig. 5. 1 as gas inlet 1, and was used to confirm by comparison the effect of the local gas supply system of the planar slit.

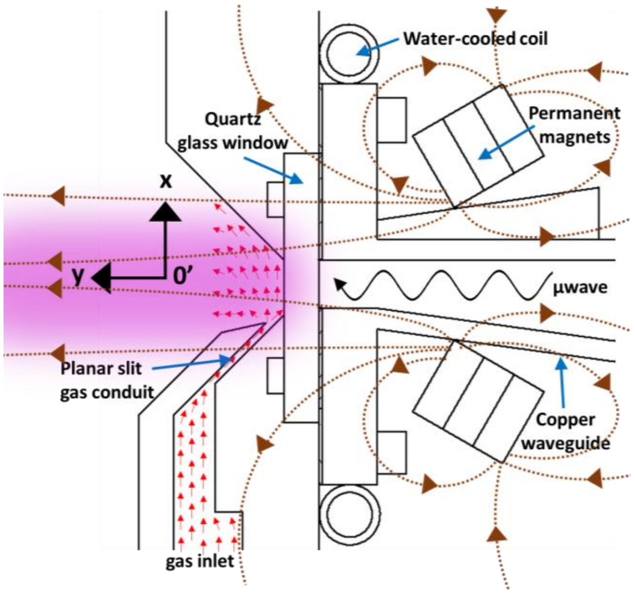

Figure 5.2: Detailed schematic of the microwave window region. The red arrows represent direction of gas flow while the brown arrows with broken lines show the magnetic field emanating predominantly from the permanent magnets. 0' is at (0 mm, -16 mm, 0 mm) position.

A set of pancake coils made of wound copper wires and powered by a DC power supply are installed around the chamber to produce a linear magnetic field inside. When combined with the Nd-Fe permanent magnets installed in the microwave inlet region, a local electron cyclotron resonance (ECR) region is generated at the plasma downstream, a few millimeter from the plasma-facing quartz window surface. Another set of weaker permanent magnets is installed in the terminal wall, opposite flange to the microwave window, to enhance the expansion of the sheet plasma across the entire drift axis. Magnetic field lines along the microwave window region in Fig. 5.2 are generated using Metamesh 4.0 as illustrated by the brown broken line arrows. Fig. 5.3a) shows *B* inside the vacuum chamber induced by adjusting the current input in the pancake coils up to 15 A. The figure shows the field intensity distribution as a function of position y, measured from the center of the plasma chamber. On the plasma-facing surface of the quartz inlet window, the field is maximum and steeply decreases down to 200 G range along the central axis of the chamber at $y = 0$. The ECR condition is achieved starting at 14 A coil current. The B at this position is shown in Fig. 5.3b) for varying coil current.

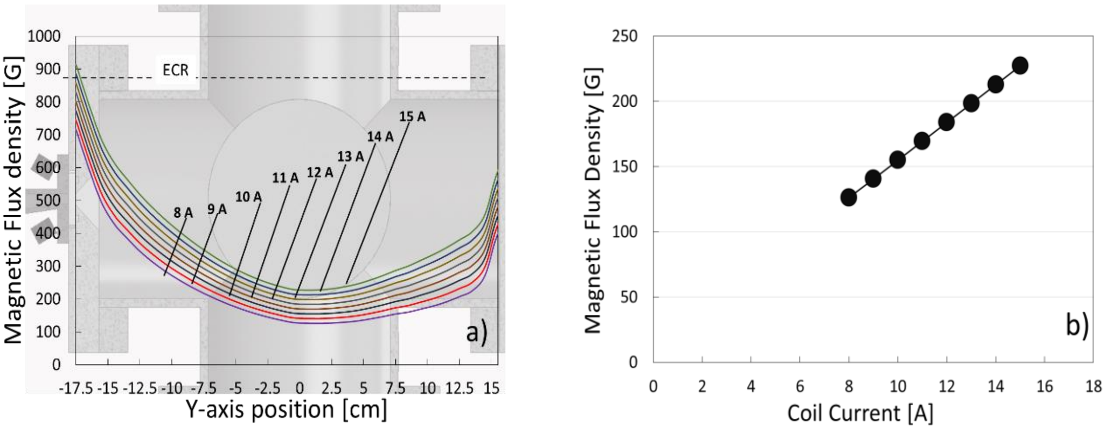

Figure 5.3: Magnetic flux density profile inside the vacuum chamber at varying coil current a) along the central drift axis and b) at y=-17.5 cm position.

Images of the discharge showing the plasma thickness were captured using a Pentax K-7 digital camera and processed using ImageJ software, as shown in Fig. 5.4). The image is converted to an 8-bit grayscale file, as in Figure 5.4a), which linearly scales the image pixels to a 0 to 255 scale representing the image contrast based on pixel brightness and plotted for each row to create a 2-D plot of the intensity profile in Fig. 5.4b).

Measurements of the electron temperature (T_e), plasma density (n_e), plasma potential (V_{plasma}) and floating potential (V_{space}) were carried out by using a 2 mm long cylindrical Langmuir probe of 0.5 mm diameter which can be moved vertically across the plasma sheet at y=0. *I-V* characteristics were recorded for varying microwave input power and magnetic flux density

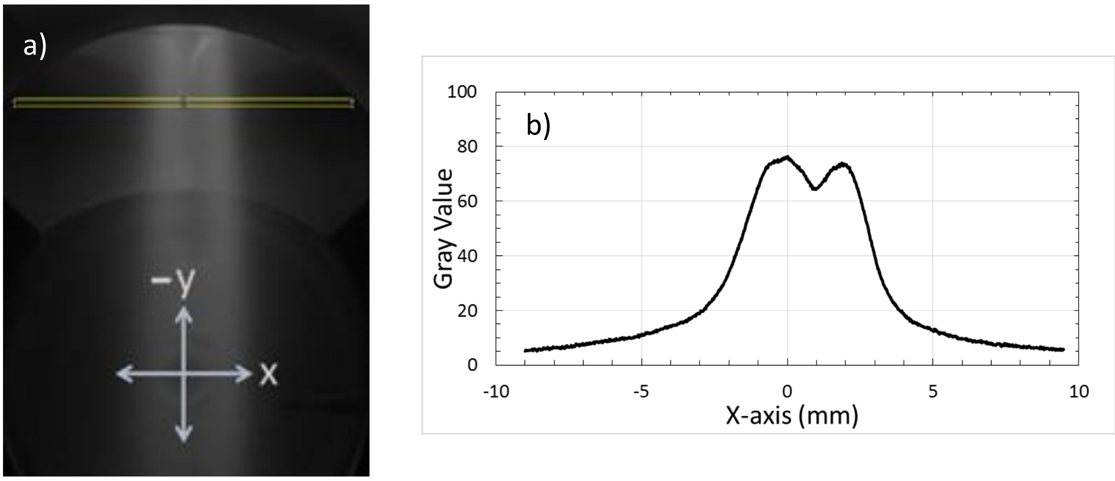

Figure 5.4: Image processing of the plasma glow showing the a) actual image in 8-bit with the highlighted region of interest, b) plotted intensity values versus the relative

5.3 Results

5.3.1 Plasma optical glow

Plots showing the Ar plasmas optical glow intensity versus the position at *x*-axis (direction of the sheet thickness) set perpendicular to the y-axis and the chamber axis for varying microwave power are shown in Fig. 5.5 for different intensities of the magnetic field. The intensity of the optical glow shows that the luminous intensity decreases towards higher magnetic field. At 0.5 kW, the optical glow appears to be more dispersed along the sheet thickness while also exhibiting the highest intensities of the plasma glow. The increased input power reduced the intensity of the plasma glow down to less than half the low power intensity at 2 kW. The observed sheet thickness which is estimated to be around 4 cm except at 0.5 kW agrees with the initial calculation of the plasma thickness from Larmor radius presented in [6]. From 1 kW, the assumed sheet thickness did not show significant reduction across the applied magnetic field.

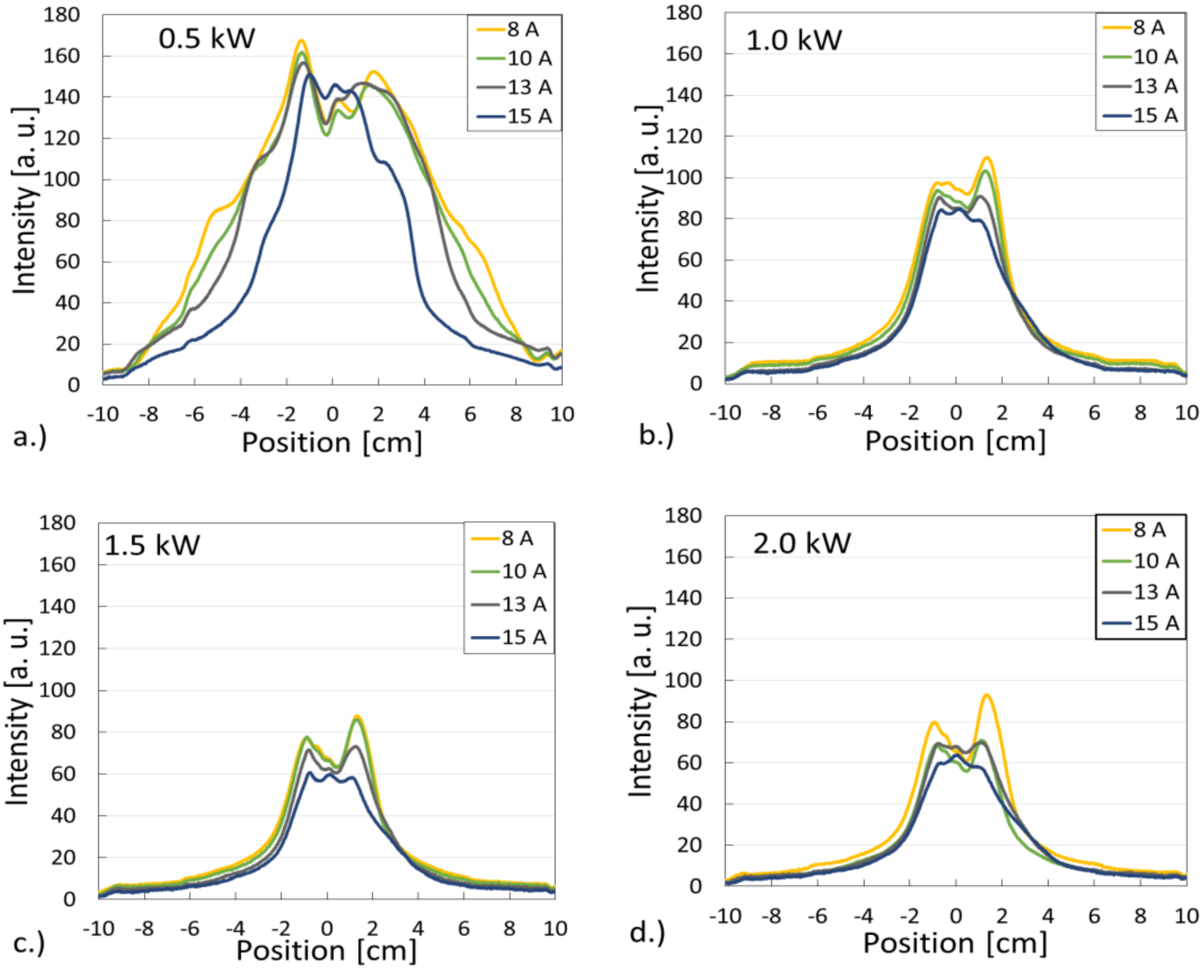

Figure 5.5: Intensity of the plasma glow of the sheet plasma images at varying coil current for P_{mw} = a) 0.5 kW, b) 1.0 kW, c) 1.5 kW, d) 2 kW across the x-axis.

5.3.2 T_e, n_e, V_{plasma} and V_F

The measured probe *I-V* traces taken at the center of the plasma chamber (x=0, *y*=0) were analyzed for T_e, n_e, V_{Plasma}, and V_F with respect to varying *B* and P_{mw} and are shown in Fig. 5.6 and Fig. 5.7. The probe location at the center of the chamber corresponds to the 17.5 cm distance from the quartz window surface. The overall behavior of T_e, in Fig. 5.6a), is largely dependent on the magnitude of the applied linear magnetic field. At a relatively low power of 0.5 kW, T_e is significantly higher than the higher input powers across the range of field intensities. For $P_{mw} \geq 1.0$ kW the measured T_e maintained the same range against increasing applied *B* and did not hint on the emergence of more energetic electron population due to the applied power in this region. The electrons at 0.5 kW appear to have higher energies than those excited at higher P_{mw}. Meanwhile, in Fig. 5.6b), n_e increases towards higher magnetic flux density.

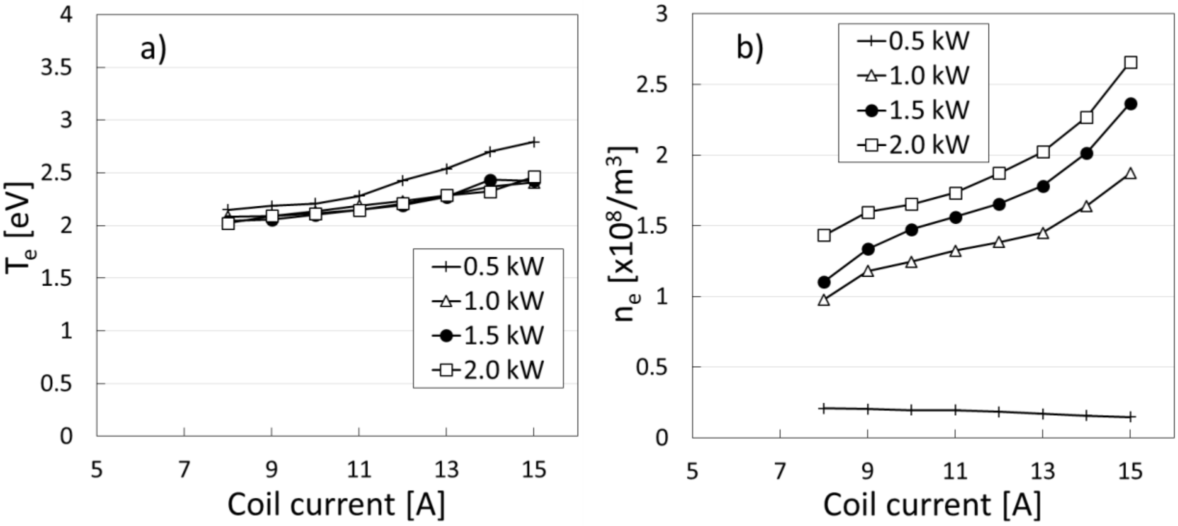

Figure 5.6: Plot of magnetic field (*B*) and microwave input power (P_{mw}) dependence of a) electron temperature (T_e), b) electron density (n_e).

The plot of the plasma potential, V_{plasma} against the magnetic field intensity is shown in Fig. 5.7a). It showed a constant increase as the current coil was increased while the floating potential, V_f values plotted in in Fig. 5.7b) become more negative with increasing coil current. In accordance with the change in electron temperature that shows only difference of 0.5 eV except 0.5 kW case, the potential difference (V_p-V_f) did not change substantially larger than 1 eV as shown in Fig. 5.7.c).

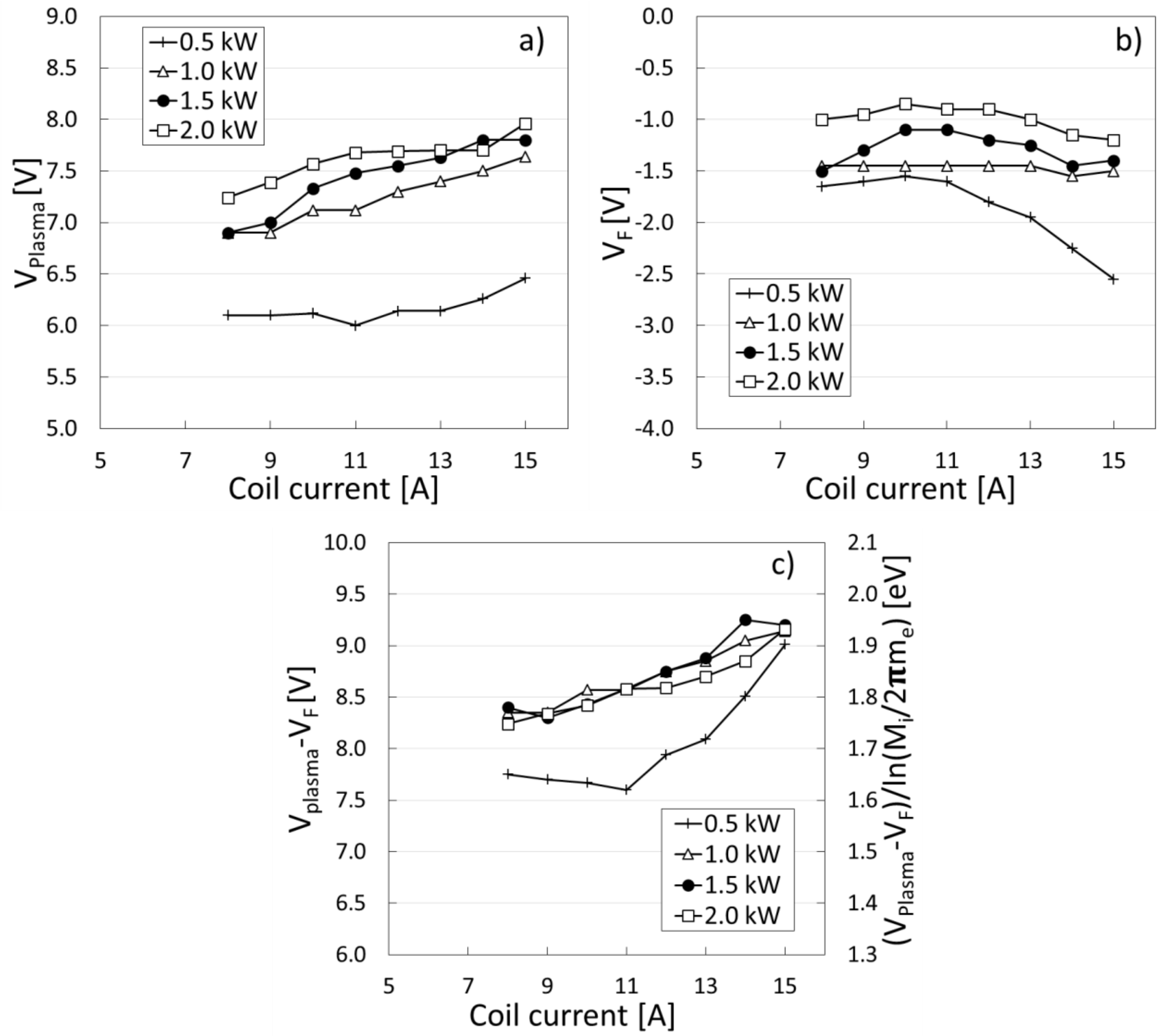

Figure 5.7: Plot of magnetic flux density (B) and microwave input power (P_{mw}) dependence of a) plasma potential (V_{plasma}) b) floating potential (V_F) and c) potential difference (V_{Plasma}-V_F) with corresponding electron temperature $(V_{Plasma}-V_F)/\ln(M_i/2\boldsymbol{\pi}\, m_e)$

5.4 Discussion

5.4.1 Change in plasma parameters

From the results of plasma parameter measurements, one sees a marked difference between 0.5 kW data and those taken at higher input power. The comparison between 0.5 kW and 1.0 kW operation shows an order of magnitude jump in electron density. For higher power operation, magnetic field intensity increased the electron density, while for 0.5 kW operation, ne decreases gradually, though not significantly, against increasing B. This may correspond to a different plasma transport from the plasma excitation region to the chamber center.

The response of the plasma against the microwave power, showing a characteristic difference at 0.5 kW as described in Fig. 5.6, can be explained by the collision frequency between charged particles and neutrals which was observed in several [8-11]. A relatively higher T_e can arise from the lower electron different configuration density. A slight increase in the positive plasma potential hints an increase in local ionization rate supported by an increase in electron density while maintaining T_e. The derived floating potential, which is more negative at 0.5 kW, indicates the higher proportion of energetic electrons at 0.5 kW.

The effect of increasing the magnetic flux density can be clearly observed by the general increase in T_e, n_e (except 0.5 kW) and V_{Plasma} while V_F becomes more negative. The increase in T_e for higher magnetic flux density agrees with the findings in [1] and [3] who attribute the effect to Joule heating arising from the decrease in plasma current cross section leading to increase in energy yield per unit volume of plasma.

5.4.2 Effect of local gas injection

In the current plasma excitation configuration, a neutral gas flow intersects the plasma irradiation onto the quartz glass window (as depicted in Fig. 5.2). To see if this "local gas injection" affects the local plasma production near the microwave window, the luminous intensity distribution, L_i, of the produced plasma near the window was observed in the procedure similar to obtain the distribution shown in Fig. 5.4. The distribution in Fig. 5.4 was compared with the distribution, L_m. taken with that discharge gas is supplied from the gas inlet 1 shown in Fig. 5.1. Expecting the cooling effect due to molecular activated recombination [12], hydrogen gas was introduced instead of Ar.

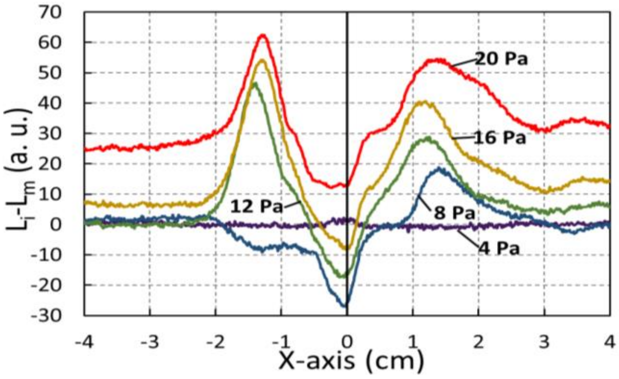

Figure 5.8: Difference in the luminosity intensities between local gas injection and gas introduced mainly into the main chamber (L_i - L_m).

First, the luminous intensity distribution (L_i) profile of the plasma at varying pressure was obtained for the case of local hydrogen gas injection in the quart window. The luminous intensity distribution profile (L_m) for the case of gas injected at the main chamber center, away from the quartz window, was also obtained and compared with that of the latter. The derived intensity profiles are similar to those shown in Fig. 5.5. From here, the intensity profile comparison, (L_i - L_m), the difference in the obtained gray values, was derived and is shown in Fig. 5.8. The plasma profiles appear to be almost similar at 4 Pa. The effect of the local gas injection can be seen as an increase in the luminous intensity of the plasma and becomes more pronounced at higher pressure, or higher flow rate. The optical emission , however, showed no indication of substantial change in the wavelength spectrum due to excited molecules.

5.4.3 Plasma instability

Measurements of the electron temperature, plasma density, plasma potential and floating potential were carried out by using a 2 mm long cylindrical Langmuir probe of 0.5 mm diameter which can be moved across the plasma sheet. A typical *I-V* trace is shown in Figure 5.9 for varying magnetic field coil current and at Figure 5.10 for different input microwave power. The effect of increasing the magnetic flux density (and microwave input power) can be observed as elevation of the electron saturation current. Similarly, an increase in the microwave power improves the electron saturation. Probe current fluctuations can be observed as it approaches saturation and intensifies in the direction of high magnetic flux whereas 1 kW input power shows the highest oscillatory amplitude, just before an abrupt increase in electron saturation from 0.5 kW. These effects were investigated by measurement of time-varying electron and ion saturation currents.

Experimental observations were conducted in the ECR sheet plasma device under imposed conditions of varying magnetic flux density and microwave input power. The saturation current was measured at a sample rate of 10kS/s equivalent to measurements of up to 5 kHz. No significant wave presence were observed beyond this frequency. From the FFT, the horizontal axis has a spectral resolution of 2.5 Hertz.

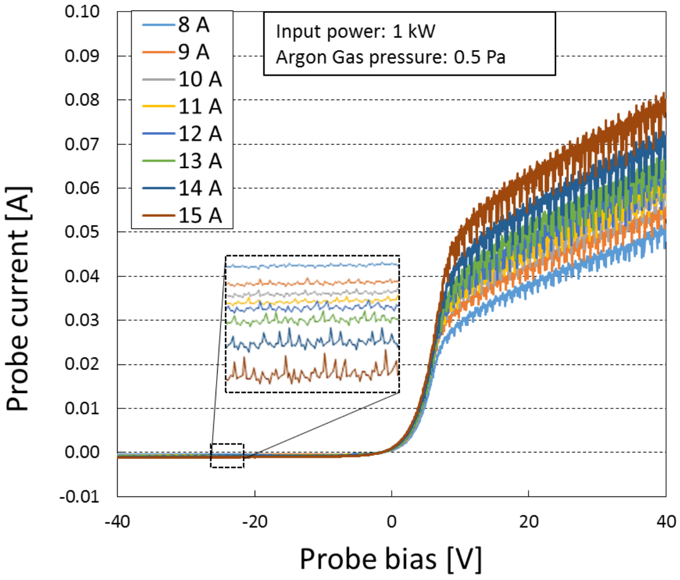

Figure 5.9 : I-V trace at varying coil current.

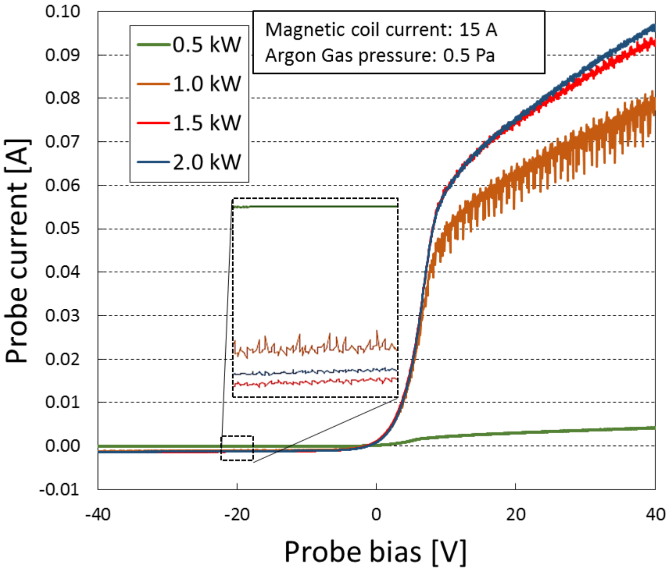

Figure 5.10 : I-V trace at varying microwave power.

The fluctuations show transitions between quasiperiodic to chaotic nature under certain tuning parameters. There are several dominant low-frequency bands observed. The input power affects the behavior of the plasma instability as shown in Fig. 5.11 to Fig. 5.14. Shown are are frequency spectra at 15 a coil current. At 0.5 kW, the low frequency instability appears as almost chaotic, as in Fig. 5.11 with a central peak below 1 kHz. When the power is increased at 1.0 kW, the instability transitions to a quasiperiodic frequency band with several lower harmonics. The strongest comes from 50-550 Hz range containing 11 periods of frequency at 50 Hz interval. The succeeding frequency bands at 750-1150 Hz while and 1350-1750 Hz are its harmonics with amplitude about a factor of half to that of the fundamental band.

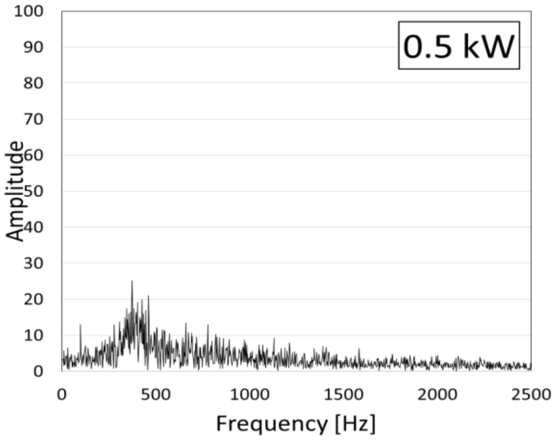

Figure 5.11: Frequency spectrum of plasma instability at 0.5 kW.

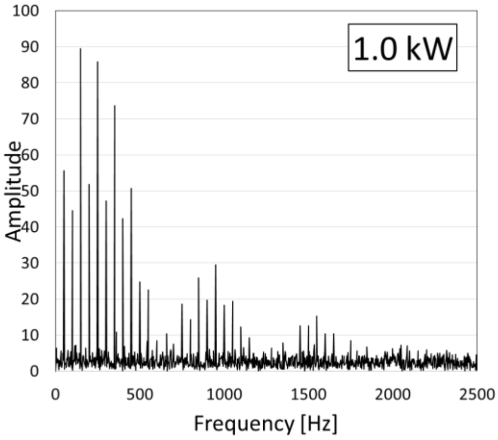

Figure 5.12: Frequency spectrum of plasma instability at 1.0 kW.

Figure 5.15 shows the frequency spectrum of plasma instability at 0.5 kW for different magnetic coil current. The instability at ECR shows relatively high amplitude of the instability at around 372.5 Hz. The amplitude of the instability abruptly decreased with the reduction of coil current while the frequency of instability moved to around 850 Hz. Meanwhile, another set of quasiperiodic instability in the lower frequency was also observed at lower current coil.

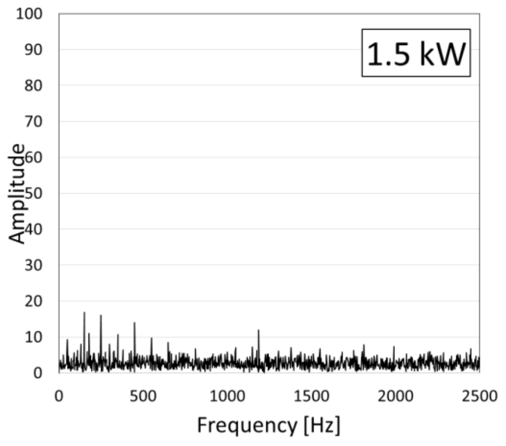

Figure 5.13: Frequency spectrum of plasma instability at 1.5 kW.

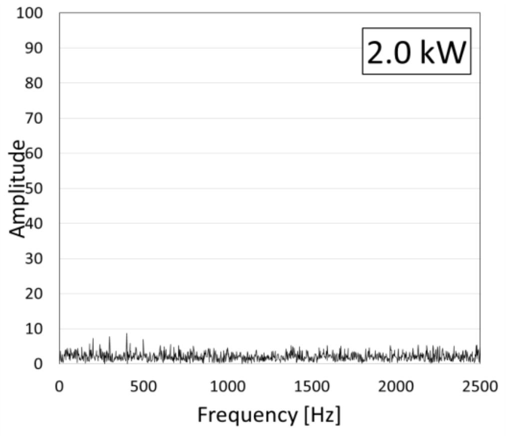

Figure 5.14: Frequency spectrum of plasma instability at 2.0 kW.

In Figure 5.16, the plot of the spectral instability is shown at different coil current values. The instability show quasiperiodic behavior with the principal peak at 350 Hz. Harmonics occur at higher frequency with lower amplitude. It can be noted that no direct trend can be extracted from the dependence of the instability to the coil current.

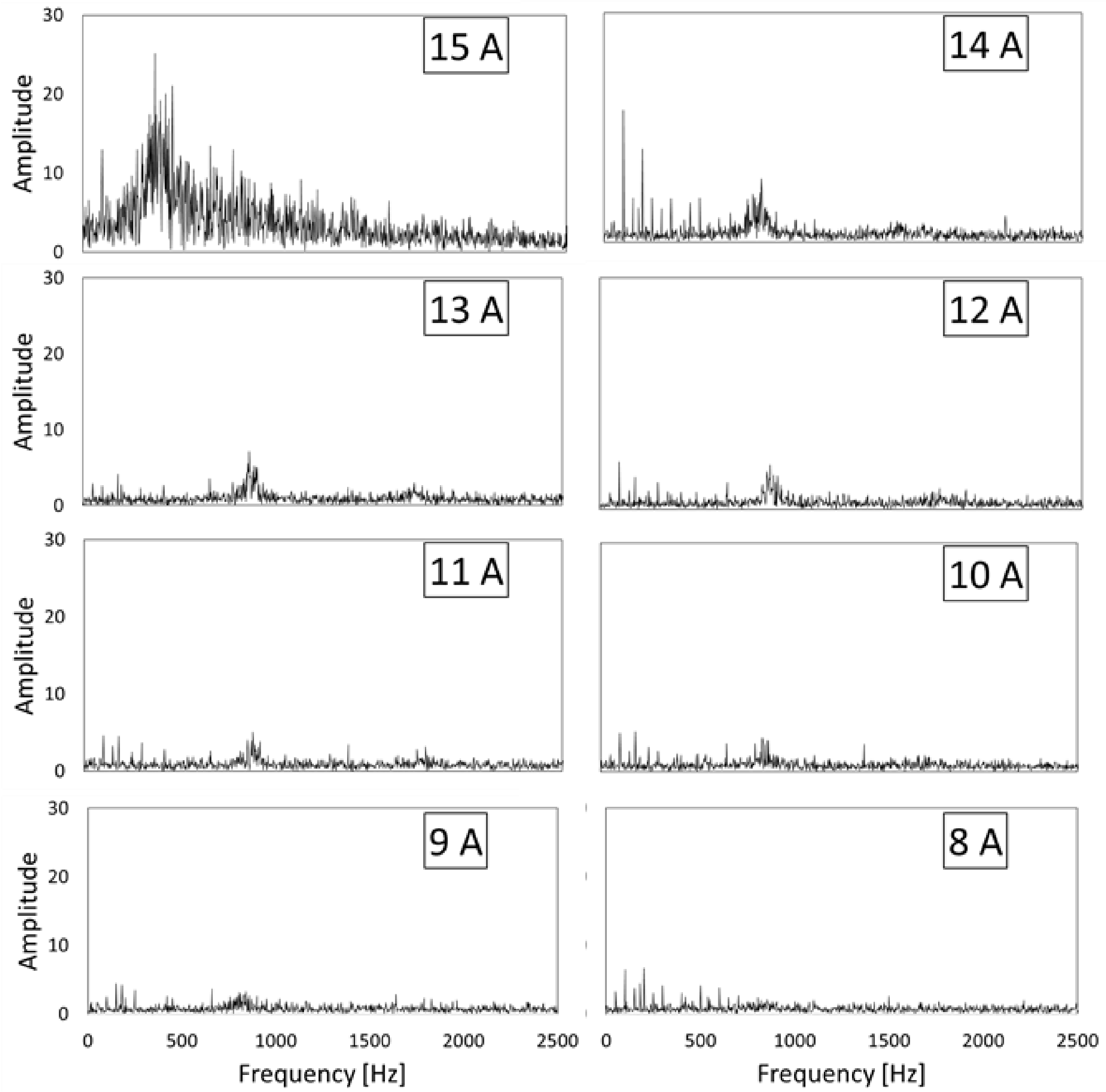

Figure 5.15: Frequency spectrum of plasma instability at varying coil current at 0.5 kW.

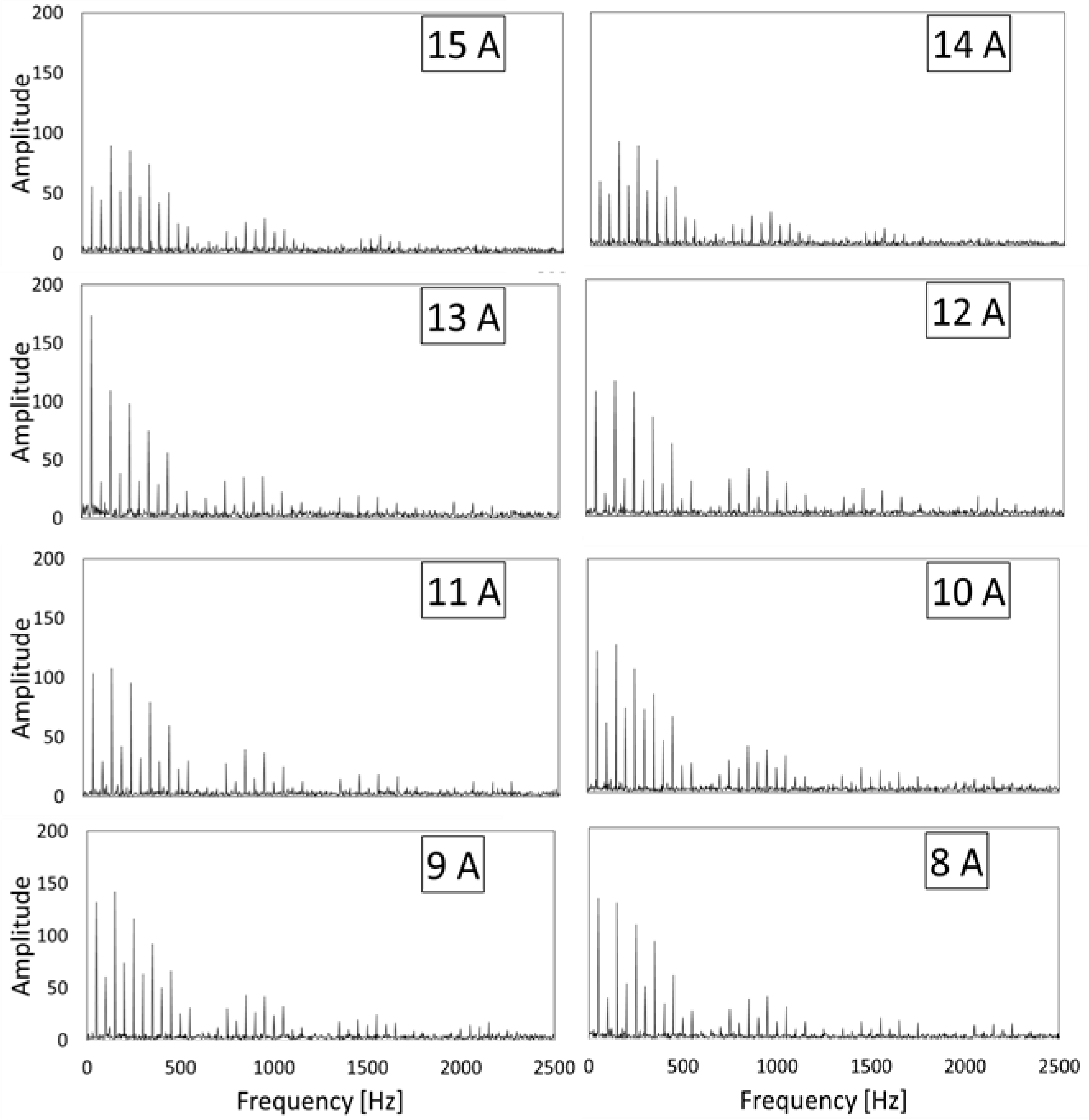

Figure 5.16: Frequency spectra of I_{sati} at varying coil current for 1.0 kW microwave input power in the sheet plasma device.

5.5 Conclusion

The effect of increasing the magnetic flux density for the microwave inlet window for a sheet plasma device with localized ECR was investigated. The electron temperature, electron density and plasma potential increased at higher magnetic field at the center, indicating better transport of plasma for the microwave excitation region. The plasma and the floating potentials, seems to suggest the presence of some high energy tail in the electron energy distribution function. Luminous intensity distributions of the plasma glow show a clear difference between two different ways to supply discharge gas: local injection at the microwave inlet and at the central region of the plasma chamber. The local injection changes the spatial distribution of the plasma optical glow due to neutral gas flow, and the effectiveness of the flow for window cooling has to be confirmed in the future study.

References

[1] I.A. Krinberg, Tech Phys. Lett. **29** (6), 504-506 (2003).

[2] E. Hashemi, K. Niayesh, H. Mohseni, Turk. J. Elec. & Comp. Sci. **24**, 4957-4969 (2016).

[3] M. Galonska, R. Hollinger, I.A. Krinberg, P. Spaedtke, IEEE T. Plasma Sci. **33** (5), 1542-1547 (2005).

[4] H.J. Woo, K.S. Chung, M.J. Lee, T. Lho, Phys. Plasmas **16**, 023505 (2009).

[5] M. Yoshida and K. Kajinishi, IEEE Trans. Plasma Sci. **31**, 40 (2003).

[6] A.R.B. Gines, M. Wada, Plasma and Fusion Research **14**, 3401085 (2019).

[7] O. Tarvainen, et al., Plasma Sources Sci. Technol. **23**, 025020 (2014)

[8] A.T.T. Mostako, et al., IEEE T. Plasma Sci. **44** (1), 7-14 (2016).

[9] S.F. Yoon, et al., Vacuum 61, 29-35, (2001).

[10] C.A. Outten, J.C. Barbour and W.R. Wampler, J. Vac. Sci. Technol. A **9 (3)**, 717-721 (1991).

[11] C. Moon, S. Tamura, T. Kaneko, R. Hakakeyama, J. Plasma Fusion Res. **9**, 436-440 (2010).

[12] N. Ohno, N. Ezumi, S. Takamura, S.I. Krasheninnikov, A.Y. Pigarov, Phys. Rev. Lett. 81, 818-821 (1998)

Chapter 6

High Energy Electrons in a Magnetized Sheet Plasma

A plasma cathode excited a millimeters thick sheet plasma throughout a 92 cm long chamber in a 270 G linear static magnetic field. Electron energy probability functions measured for Ar plasmas by an electrostatic probe indicated the presence of high energy electrons in the produced plasma. The high energy electron component occupied the substantial part of the electron energy distribution function at lower plasma operating pressure. Electrical bias voltage applied to the electrode terminating the plasma flow determined the plasma space potential.

6.1 Introduction

In the present design of the microwave sheet plasma, we found that the present configuration does not promote the acceleration of higher energy electrons and the design does has no provision for this mechanism. Uramoto [1] suggested the presence of high energy electrons in his sheet plasma configuration, and presence of the high energy electrons in a plasma is often desirable for some applications of plasma processes. Any modification in the present design may be done based upon the study derived from this chapter.

Proper magnetic field structure realizes good plasma confinement as well as flux distribution of desired species for processing applications. Uramoto demonstrated that negative hydrogen (H^-) ions can be produced efficiently by shaping a plasma to a thin sheet by coupling a pair of permanent magnets and a linear magnetic field[1]. This magnetic field configuration concentrates high energy electrons in the plasma sheet, while a low electron temperature plasma surrounds the sheet. The negative hydrogen ions were supposed formed by dissociative electron attachment to vibrationally excited molecules produced in high energy electron region. Namely, high energy electrons, e_f, excite hydrogen molecules to high rotationally and vibrationally excited states, H_{2v}^*, by collisions in the thin layer of electron flowing channel.

$$H_2 + e_f \to H_{2v}^* + e_f' \qquad (6.1)$$

More than 12 eV electron energy makes the cross sections for the above reaction substantial. Neutral excited molecules H_{2v}^* leave high energy electron channel to be H^- through collisions with low energy electrons, e_s.

$$H_{2v}^* + e_s \to H + H^- \qquad (6.2)$$

The produced H^- are easily destroyed by high energy electrons, and thus, the sheet plasma configuration localizing the high energy electron channel is ideal to make a H^- ion source.

The original configuration employed a plasma cathode that made the stable excitation of reactive plasmas possible[3]. It is highly probable that a double layer exists between inside and outside of the hollow cathode contained in the plasma cathode. While another double layer may bridge the plasma cathode compartment and the downstream plasma, accelerating electrons from the plasma cathode. Uramoto suggested the presence of high energy electrons in his sheet plasma configuration[4], and presence of the high energy electrons in a plasma is often desirable for some applications of plasma processes. In this paper, the electron energy probability function (EEPF) was measured to see the existence of high energy electrons in a downstream plasma by inserting a small Langmuir probe into a low power density sheet plasma.

6.2 Experimental methods

6.2.1 Plasma cathode

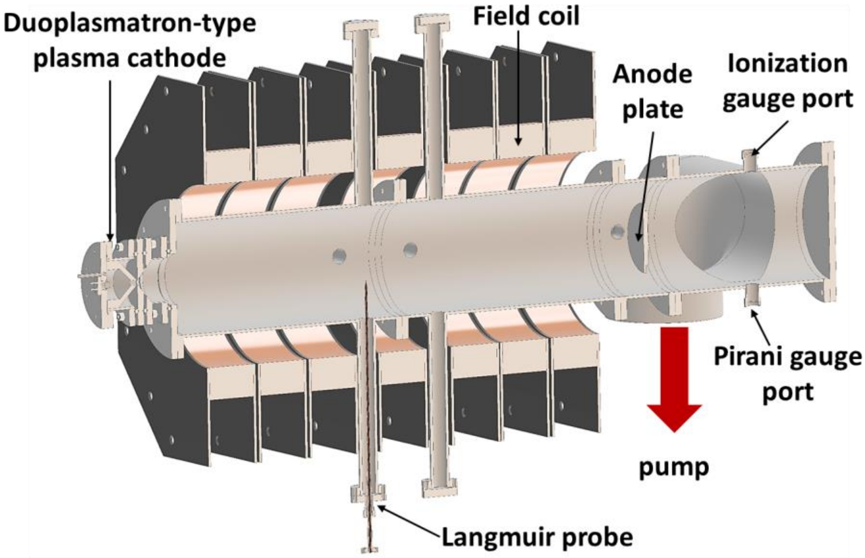

Figure 6.1: Schematic diagram of the experimental apparatus.

Figure 6.1 shows the experimental arrangement. A 21 cm diameter 92 cm long stainless steel chamber served as a container for a sheet plasma. Seven coils form a linear magnetic field along the axis over 90 cm length. A plasma generated from the plasma cathode flows in the chamber, and terminated by the end plate. The end plate contains a permanent magnet, and can be biased at any voltage with respect to the chamber wall. A 1,500 ℓ/s turbo-molecular pump evacuates the system down to a pressure less than $6X10^{-5}$ Pa.

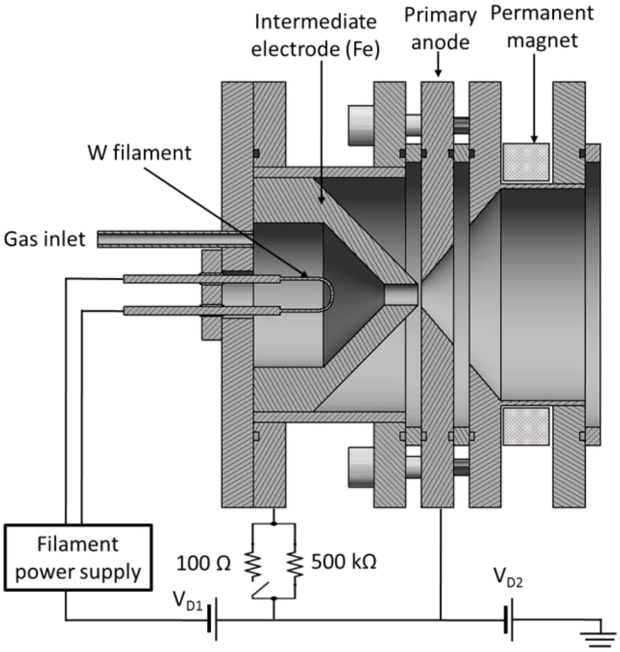

Figure 6.2: Arrangement of the plasma cathode. In the figure, V_{D1} and V_{D2} indicate primary discharge supply and the secondary discharge power supply,

The details of the plasma cathode structure are given in Fig. 6.2. A 7 cm long 0.4 mm diameter tungsten filament creates discharge current by the thermionic electron emission. The shape of the conical intermediate electrode compresses plasma produced by the hot filament cathode, while the concentrated magnetic field at the muzzle of the iron intermediate electrode magnetically constricts the plasma flow to enhance ionization. Electrons are extracted from the plasma maintained by the primary discharge voltage, V_{D1}, between the anode and the filament cathode. The plasma is further extracted by the secondary discharge voltage, V_{D2}, applied between the anode and the grounded downstream chamber. After passing through the chamber in the linear magnetic field, the plasma touches down to the end plate.

There is the plasma expansion chamber between the anode of the primary discharge and the downstream chamber. This chamber is electrically isolated from the other parts of the discharge circuit and is left floated during plasma operation. The plasma ignition switch indicated in Fig. 6.2 is closed to commence a discharge, but is opened when a stable primary discharge is established through controlling the filament heating current. Once the stable plasma is established in the primary discharge circuit, secondary discharge automatically starts with the secondary discharge voltage.

6.2.2 Probe diagnostics

A 2 mm end part of a 0.6 mm diameter tungsten wire is used as an electrostatic probe tip. An alumina tube covers the unexposed part of the tungsten wire, while a grounded copper tube outside of the alumina tube electrostatically shields the probe signal line from surrounding noise. Another larger diameter alumina tube contains the copper tube to protect the probe from plasma radiation. A source measure unit, Yokogawa model GS610, records the probe *I-V* characteristics as digital data. The second derivative of the measured probe current, I_p, with respect to the probe voltage, V_p, yields the electron energy distribution function, $F(\boldsymbol{\varepsilon})$, for energy $\boldsymbol{\varepsilon}=eV_p$ through the equation

$$F(\varepsilon)=\frac{4}{eS_p}\sqrt{\frac{mV_p}{2e}}\frac{d^2I_p}{dV_p{}^2} \tag{6.3}$$

with e, S_p, and m being electronic charge, probe surface area and electron mass, respectively [5]. The second derivative is proportional to electron energy probability function (EEPF), which should show a straight line for Maxwell distribution with the slope corresponding to electron temperature[6]. Therefore, the high energy electron components in a sheet plasma is discussed in terms of normalized EEPF.

6.2.3 Experimental procedure

The magnetic field intensity was adjusted to 270 G, because the intensity realized the minimum plasma sheet thickness as thin as 3 mm confirmed with hydrogen gas operation. The corresponding sheet plasma width was confirmed wider than 16 cm. The power supply regulated the primary discharge voltage to be 40 V by a feedback control for the hot cathode. The secondary discharge power supply fixed the secondary discharge voltage to 60 V throughout the experiment. The end plate was biased from 0 to 80 V, while Ar pressure was adjusted from 3 mPa to 25 mPa. The sweep of the probe bias voltage started from 25 V to reach -75 V.

6.3 Results and discussion

6.3.1 Plasma cathode performance for Ar

The plasma cathode should establish enough density to cause secondary discharge. The secondary discharge transports enough particle flux toward the downstream chamber, which should appear in the current flowing through the end plate electrode. When the pressure in the small intermediate electrode is not enough, the electron current from the hot filament directly hits the electrode without ionizing collision, and the secondary discharge current does not become larger than the primary discharge current. To see the minimum pressure for the proper operation of the plasma cathode with Ar, the ratio of the secondary discharge current to the primary discharge current, I_{D2}/I_{D1}, the ratio of the end plate current to the primary discharge current, I_{plate}/I_{D1}, and the floating potential of the chamber inserted in between the intermediate electrode and the downstream chamber, V_F,

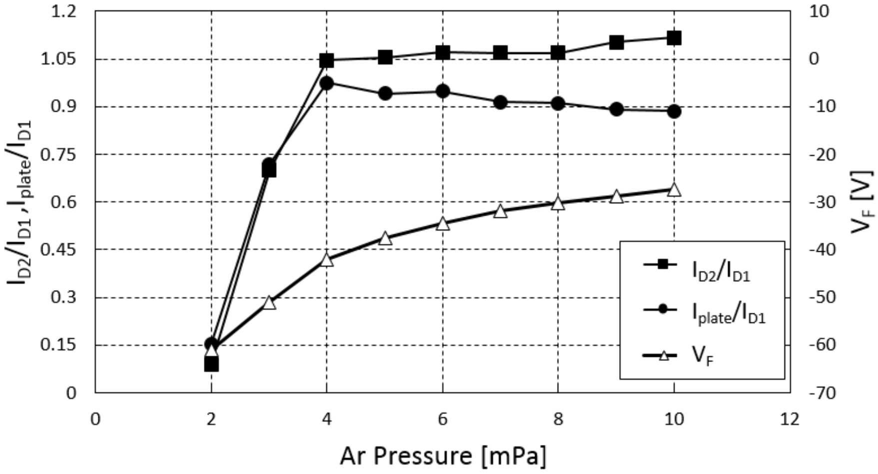

Figure 6.3: Discharge current ratio I_{D2}/I_{D1}, the ratio of the end plate current to the primary discharge current, I_{plate}/I_{D1}, and the floating potential of the chamber inserted in between the intermediate electrode and the downstream chamber, V_F, plotted as functions of Ar pressure.

were measure as functions of Ar pressure. The results are shown in Fig. 6.3. As shown in the figure, the discharge current ratio saturated around 4 mPa downstream chamber pressure. In accordance with the saturation of the discharge current ratio, the discharge current reaching the end plate also saturated around 4 mPa. The ratio of end plate current to the primary discharge current was almost 100% at 4 mPa, but slightly decreased down to 90% as it reached 10 mPa Ar pressure.

The floating potential, V_F plotted together with the discharge current ratios in Fig. 6.3 gives the hint how the primary electrons from the hot W cathode are thermalized. In the chamber connecting the primary discharge anode and the downstream chamber, there exists the electrons directly coming from the primary discharge cathode, or the W filament. The filament was biased at -100 V with respect to the electrically grounded downstream chamber, and the floating potential can be as high as this value. The floating potential approached close to the ground potential, as the pressure was raised to increase the frequency of the ionization event. The measured V_F dependence upon pressure showed a transition around 7 mPa as shown in Fig. 6.3, with saturating trend at higher pressure.

Within the pressure range where stable plasma operation is achieved, the plate current equivalent to the discharge current running through the downstream chamber took the maximum at around 30 mPa and minimally decreased with the increasing pressure as shown in Fig. 6.4. The ratio of the plate current to the ion saturation gradually decreased above 4 mPa, while the measured ion saturation current by the probe biased at -75 V constantly increased with increased Ar pressure. The efficiency of the plasma cathode to produce sheet plasma improves due to increased ionization events at relatively higher pressure.

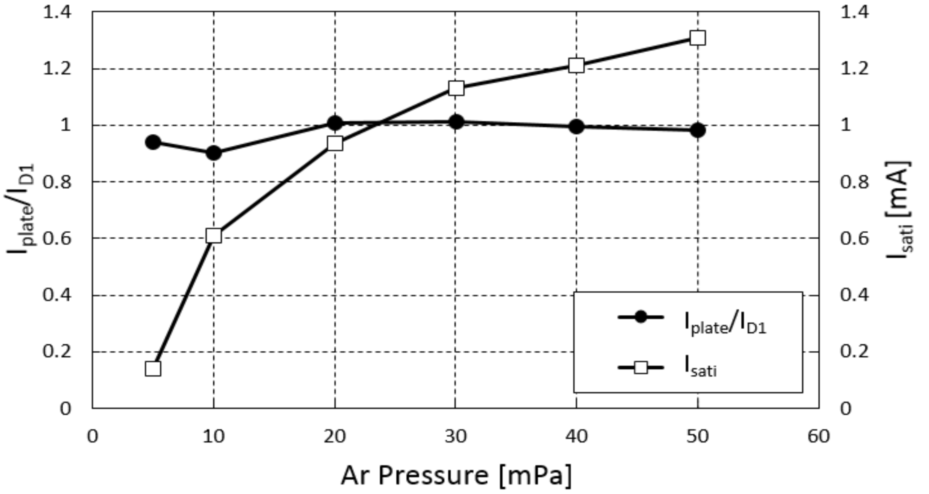

Figure 6.4: Dependence of end plate current, I_{plate} and that of ion saturation current I_{sati} upon Ar pressure in the downstream chamber.

6.3.2 EEPF dependence upon Ar pressure

Typical EEPFs obtained from probe *I-V* characteristics for corresponding pressure are shown in Fig. 6.5. Plots show linear parts in the low electron energy region, indicating the electron energy distributions fit well to Maxwell distribution functions. From the low electron temperature component of 2.7 eV at 50 mPa the temperature is increased to 2.92 eV, 3.34 eV and 3.6 eV as the Argon pressure was reduced to 30 mPa, 10 mPa and 5 mPa, respectively. As pressure is increased, more and more energy is transferred from electron to plasma species during inelastic collision. The substantial part of electrons belonged to Maxwellian part of the distribution function, and the non-Maxwellian part did not exceed more than several percent of the entire population. A "bump on tail" type distribution function appeared at lower pressures. Similarly, the high energy tail depletes to lower energies at higher pressures due to inelastic collisions.

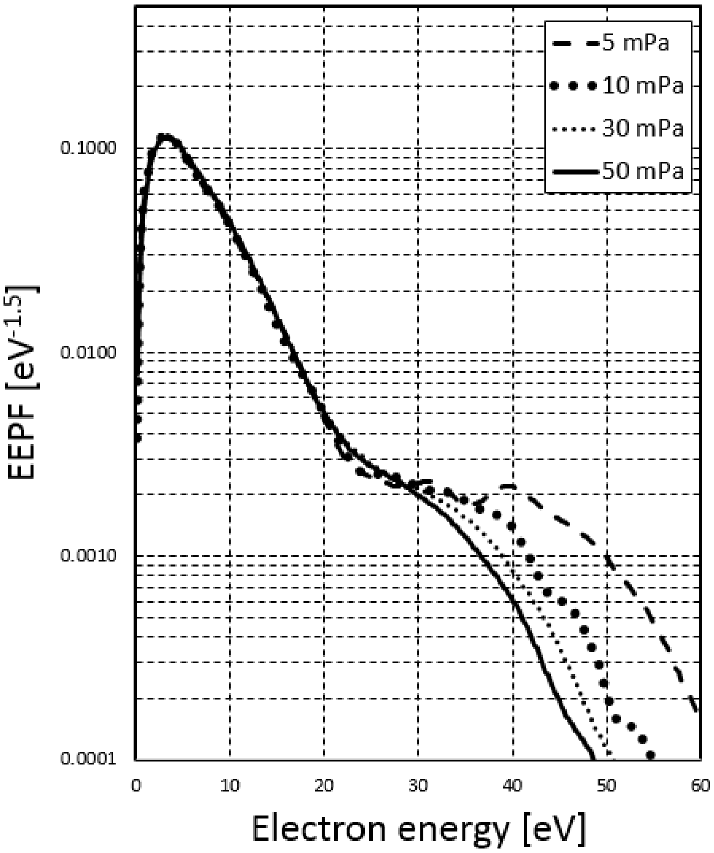

Figure 6.5: Electron energy probability function for different Ar pressure.

6.3.3 EEPF dependence upon end plate voltage

The plasma space potential of the plasma sheet can be controlled by tuning the voltage applied to the end plate. In Figure 6.6, a typical I-V trace obtained with a Langmuir probe shows the translation of trace toward the positive horizontal axis at the same magnitude as the applied bias from 0 V. Figure 6.7 shows the dependence of plasma potential measured by the probe upon the end plate voltage. A straight line in Fig. 6.7 represents the condition that the end plate voltage is equal to the plasma space potential. The measured plasma space potential is almost the same as the end plate voltage, except the case that the end plate was biased at the ground potential and at 80 V. For these exceptions, the plasma space potential is greater than 1.7 V and less than 1.4 V at 0 V and 80 V, respectively.

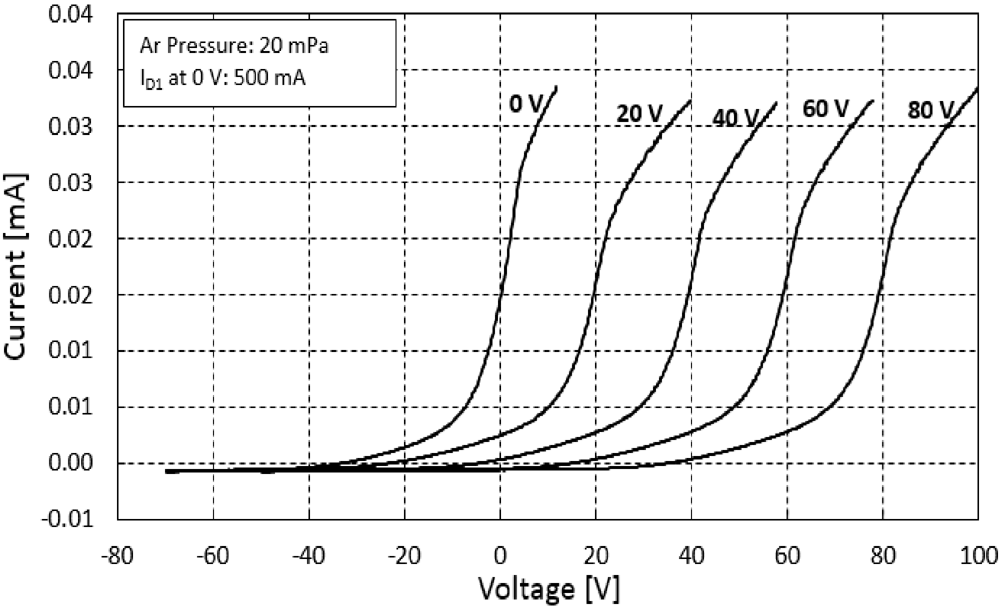

Figure 6.6: I-V trace at varying applied end-plate

Starting at ground potential, induction of positive potential to the end plate up to 80 V enhanced the higher energy electron components of the plasma. Positive bias to the end plate made the electron temperature higher to 4.09 eV at 40 V and 4.98 eV at 80 V from

3.36 eV at ground potential. EEPF of corresponding end plate voltage is shown in Figure 6.8.

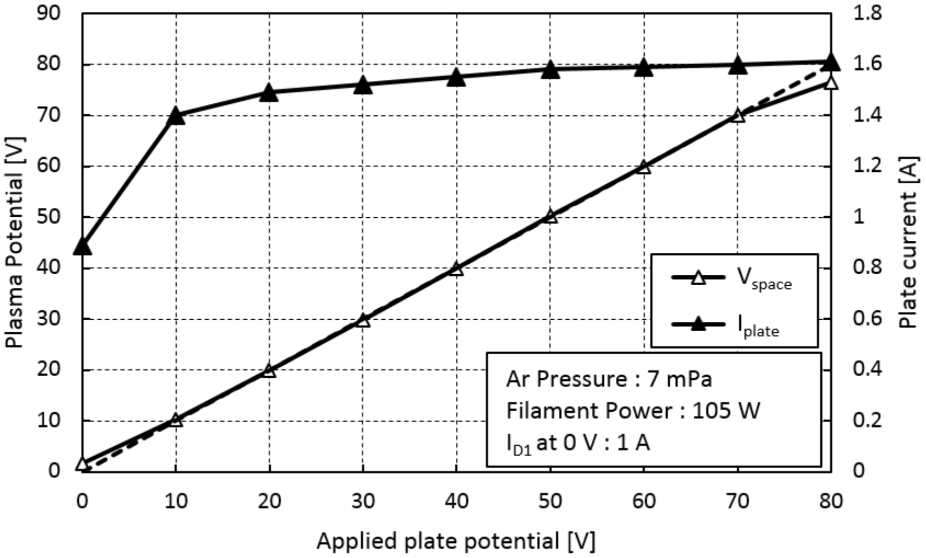

Figure 6.7: Dependence of plasma space potential, V_{space}, and that of end plate current, I_{plate}, upon bias voltage applied to the end plate. A solid line is drawn to guide readers' eyes for showing the condition of V_{space} = plate voltage.

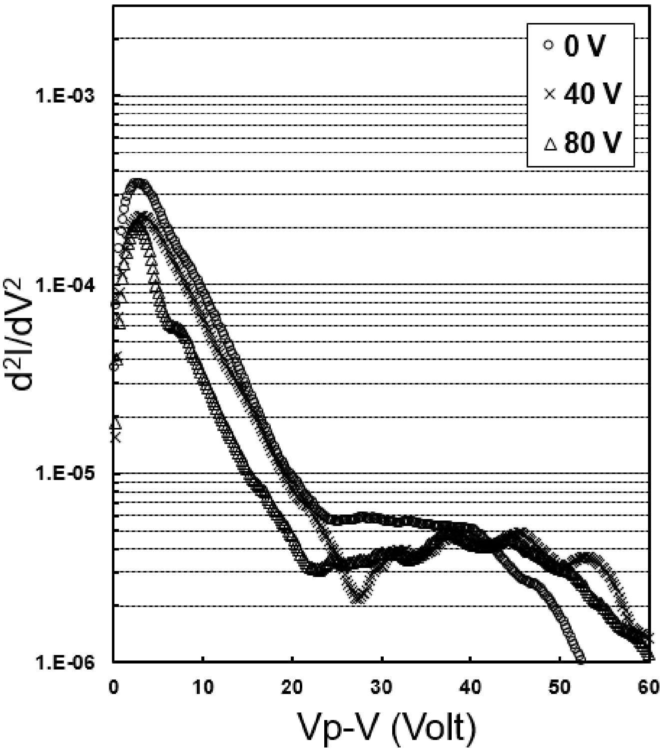

Figure 6.8: Plot of d^2I/dV^2 at varying end plate bias.

6.4 Conclusion

A sheet plasma excited by a plasma cathode contains high energy electrons as predicted by Uramoto. The relative density of the high energy electrons increased with the decrease of the plasma operation pressure. The plasma space potential of the sheet plasma can be easily changed by controlling the electrical potential of the electrode that terminates the plasma flow along the linear magnetic field at the side confronting to the plasma cathode. The lowest pressure that supported the adequate ionization of the cathode plasma enabled a stable operation of the sheet plasma with a high energy electron component.

References

[1] J. Uramoto: AIP Conference Proceedings, **158**, 319 (1987).

[2] A. Ando, T. Kuroda, Y. Oka, O. Kaneko, A. Karita, T. Kawamoto: Rev. Sci. Instrum. 61, 442 (1990).

[3] J. Uramoto: Shinku (in Japanese) **28**, 701 (1985).

[4] J. Uramoto: Shinku (in Japanese) **31**, 4 (1988).

[5] C. Gutierrez-Tapia and H. Flores-LLamas, Phys. Plasmas, **11**, 5102 (2004).

[6] V. A. Godyak and B. M. Alexandrovich, J. Appl. Phys. 118 233302 (2015).

Chapter 7

Conclusions

A 2.45 GHz sheet plasma device was developed for possible industrial application in surface technology. It features several novel parts including a tapered waveguide, a set of permanent magnets and field coils to generate a local ECR region as well as contain the plasma into a sheet plasm configuration, a local gas injection in the cathode region which enables high power operation. Overall, the design achieved several advantages:

7.1 Achievements

1. A stable discharge is attained using a cathodeless system.
2. The device can be operated at high microwave input power for a couple of hours without observing any excessive heating. Stable plasma is even achieved up 3 kW for several minutes.
3. The local ECR condition from the combined field coils and permanent magnets contributes to enhance plasma excitation efficiency.
4. The production of high density gradient plasma can be optimized by the magnetic field coils and input power.
5. High energy electrons can be attained by addition of end-plate bias.

7.2 Future device improvement

1. Plasma instabilities were observed and further study must be performed to improve the discharge.
2. The design of the magnetic field coils needs further improvement to enable higher field.
3. Minimal distortion of the copper waveguide was observed. The design may be improved to incorporate a more rigid material.